NASA CONTRACTOR REPORT

NASA CR-2587

NASA CR-2

SUPERSONIC TURBULENT BOUNDARY-LAYER FLOWS WITH MASS INJECTION THROUGH SLOTS AND/OR POROUS WALLS, FINAL REPORT

Alvin L. Murray and Clark H. Lewis

Prepared by
VIRGINIA POLYTECHNIC INSTITUTE AND STATE UNIVERSITY
Blacksburg, Va. 24061
for Langley Research Center

NATIONAL AERONAUTICS AND SPACE ADMINISTRATION • WASHINGTON, D. C. • SEPTEMBER 1975

1. Report No.	2. Government Accession No.	3. Recipient's Catalog No.
NASA CR-2587		

4. Title and Subtitle	5. Report Date
SUPERSONIC TURBULENT BOUNDARY-LAYER FLOWS WITH MASS INJECTION THROUGH SLOTS AND/OR POROUS WALLS	September 1975
	6. Performing Organization Code

7. Author(s)	8. Performing Organization Report No.
Alvin L. Murray and Clark H. Lewis	
	10. Work Unit No.

9. Performing Organization Name and Address	11. Contract or Grant No.
Aerospace and Ocean Engineering Department Virginia Polytechnic Institute and State University Blacksburg, Virginia 24060	NGR-47-004-106
	13. Type of Report and Period Covered Contractor Report

12. Sponsoring Agency Name and Address	14. Sponsoring Agency Code
National Aeronautics and Space Administration Washington, DC 20546	

15. Supplementary Notes

Technical Monitor: Ivan E. Beckwith
Final Report

16. Abstract

An implicit finite-difference method was used to solve the compressible boundary-layer equations. The method was used to study the effects of mass transfer through porous plates, slots, and a combination of the two. The effects of the external pressure field were also included by using a global pressure interaction scheme. Two different eddy viscosity models were used for the slot and slot-porous combination cases. One was a two-layer model with inner and outer laws. The other was a multi-layer model with as many as five separate layers. Results of the present method were compared with experimental data at a Mach number of 2.8. Comparisons of the skin friction reduction and Mach number profiles gave good to excellent agreement. Pressure interaction had little effect on the slot injection skin friction but increased the skin friction of the porous and slot-porous combination markedly.

17. Key Words (Suggested by Author(s))	18. Distribution Statement
Slot injection Porous wall injection Supersonic turbulent boundary layer	Unclassified-Unlimited Subject Category 34 Fluid Mechanics and Heat Transfer

19. Security Classif. (of this report)	20. Security Classif. (of this page)	21. No. of Pages	22. Price*
Unclassified	Unclassified	83	$4.75

*For sale by the National Technical Information Service, Springfield, Virginia 22161

TABLE OF CONTENTS

LIST OF FIGURES

NOMENCLATURE

a_m, a_s	eddy viscosity constants
A^+	term in Van Driest damping factor
A_j	area of the injection device, ft^2
C	density-viscosity product ratio, $\rho\mu/(\rho_e\mu_e)$
C_f	mass fraction of the freestream species
C_{f_∞}	skin-friction coefficient based on freestream conditions
C_i	mass fraction of species i
C_p	specific heat of perfect gas, $m^2/(sec^2\text{-}^oK)$
D_{12}	binary diffusion coefficient, m^2/sec
F	tangential velocity ratio, u/U_e
$\tilde{f}$	form factor in multi-layer eddy viscosity model
g	stagnation enthalpy ratio, H/H_e
H	stagnation enthalpy, m^2/sec^2
H_k^*	δ_k^*/θ_k
h	static enthalpy, m^2/sec^2
K	eddy viscosity constant, 0.4
L	reference length, m or cm
Le	molecular Lewis number
Le_t	turbulent Lewis number
ℓ	mixing length, m or cm
ℓ_b	freestream mixing length
ℓ_m	mixing region mixing length
ℓ_s	slot mixing length

M	Mach number
$\dot{m}$	$\rho_j u_j A_j$
p	pressure, N/m^2
Pr	molecular Prandtl number
Pr_t	turbulent Prandtl number
R	gas constant
Re	Reynolds number
s	slot height, m or cm
T	temperature, ^oK
t	slot lip thickness, m or cm
u, U	tangential velocity component, m/sec
u_f	friction velocity, $(\tau_w/\rho)^{1/2}$
u^+	tangential velocity in law of the wall variables, u/u_f
V	transformed normal velocity
v	normal velocity component, m/sec
$\tilde{W}$	width of the mixing region
w	weighting factor
x	distance along surface, m or cm
y	distance normal to surface, m or cm
y^+	normal coordinate in law of the wall variables, $y\ u_f/\nu$
y_f	y at $\tilde{Z} = 0.99$
y_m	y at $\tilde{Z} = 0.5$
y_n	y at $\tilde{Z} = 0.01$
Z	mass fraction, C_i/C_{i_e}

$\tilde{Z}$	Normalized mass fraction ratio, $(C_i - C_{i,w})/C_{i,e} - C_{i,w})$
β	pressure gradient parameter, $\frac{2\xi}{u_e}\frac{du_e}{d\xi}$
γ	Klebanoff intermittency factor
δ	boundary-layer thickness
δ_o	boundary-layer thickness on flat plate
δ_r	$\delta_o + t + s$
δ^*	boundary-layer displacement thickness
δ_k^*	incompressible boundary-layer displacement thickness
ε	eddy viscosity
ε^+	ε/μ
ε_{VD}	Van Dyke parameter $(\rho_\infty^* U_\infty^* L^*/\mu_{ref}^*)^{-1/2}$
η	Levy-Lees normal coordinate
θ_k	incompressible boundary-layer momentum thickness
μ	viscosity
ξ	Levy-Lees streamwise coordinate
ρ	density
τ_w	shear stress at wall, $\mu\left[\frac{du}{dy}\right]_w$

Subscripts and Superscripts

e	condition at outer edge of boundary layer
i	species i
s	denotes limits of integration for δ_k^* and θ_k from y_n to δ
w	condition at wall boundary

o	stagnation condition, flat plate conditions
ξ	differentiation with respect to ξ
∞	freestream condition
$( )'$	differentiation with respect to η
$( )^*$	dimensional quantity
j	injectant conditions

I. INTRODUCTION

In recent years, injection of a fluid into the boundary layer has been studied both numerically and experimentally as a technique for thermal protection and skin friction reduction. Two of the most common injection configurations studied have been the porous wall and the tangential slot. In the former configuration, air or a foreign gas is injected into the boundary layer through a porous section of the wall. The tangential slot consists of a step in the wall through which the injectant enters the boundary layer parallel to the freestream flow.

Spalding and Patankar (Ref. 1) were able to obtain a solution for the tangential slot by using two regions for the flow field. In the first region, the flow was treated as a mixing of two planar flows and the wall region of the flow was neglected. When the mixing region had spread to the wall, the standard solution procedure for a turbulent boundary layer was used. With this model, Spalding and Patankar obtained good predictions of the effects of slot injection at some distance downstream, but predictions of the effects in regions near the slot were not as good.

Beckwith and Bushnell (Ref. 2) developed a finite-difference method which could be used near the slot as well as far downstream. This method used a modified form of the eddy viscosity expression developed by Bushnell (Ref. 3). In this expression, the Prandtl mixing length in the region near the slot was adjusted to account for the effects of slot injection. The mixing length in the mixing region downstream of the slot lip was proportioned to the width of the mixing region and thus increased downstream as the region spread between the slot and freestream flows. By adding the species conservation equation to the system of governing equations (Ref. 2), the growth of the mixing region was calculated and used to compute the mixing length. The method of Ref. 2 was limited to the case where the injected species was the same as the external flow.

Miner and Lewis (Ref. 4) presented a finite-difference method for predicting compressible, turbulent boundary-layer flows with tangential slot injection. Inclusion of the species conservation equation allowed predictions of the mixing between the slot and freestream flows and use of the Beckwith-Bushnell eddy viscosity model. Comparisons with the experimental data of Kenworthy and Schetz (Ref. 5) were made for three eddy viscosity models to test the accuracy of the predictions in a region near the slot. The method also contained a procedure to predict the effects of the interaction between the boundary-layer displacement thickness and the external pressure field.

In a later work (Ref. 6), Miner and Lewis extended their method to include non-reacting foreign gas injection. With a foreign gas as the injectant, the single species gas property model had to be replaced by a binary gas model. The properties used in the binary gas property model are given in Ref. 6.

Experimental studies of this problem have been conducted by a number of authors. McRee, et al. (Ref. 7) considered the effects of normal injection and slot injection on the skin friction at Mach 3. Cary and Hefner (Refs. 8, 9) studied the effects of tangential-slot injection on the film-cooling effectiveness and skin friction in a hypersonic flow of Mach 6. Finally, Kenworthy and Schetz (Ref. 5) conducted an experimental study of slot injection into a Mach 2.4 freestream.

The present study used a finite difference method to compare the effectiveness of slot injection, porous injection, and a simple combination of the two in reducing the skin friction. Comparisons are made with experimental data from a similar study by Schetz and Van Overeem (Ref. 10). The conditions for the experimental study were Mach 2.9, P_o = 69.9 N/cm^2 (100 psia), and T_o = 294 ^oK (530 ^oR). The data taken for comparison included wall-pressure distributions, Mach number profiles and pitot pressure profiles at four axial stations and wall shear as measured by a

floating element balance. Wall shear data were also taken by two Preston tubes with diameters of 0.241 cm and 0.073 cm.

The finite-difference method developed by Miner and Lewis (Ref. 4) was used in the present work. Calculations of the skin friction with and without pressure interaction effects were made using the two-layer eddy viscosity model. For the slot and slot/porous configurations, the multi-layer eddy viscosity model of Beckwith and Bushnell was also used for comparisons. Mach number profile calculations downstream of the slot were made and compared with the experimental data.

Finally, the finite-difference method was used to study the effect of combined slot-porous injection configurations on reducing the skin friction. Effects of pressure interaction and the differences in the two eddy viscosity laws were also considered.

II. ANALYSIS

The equations for two-dimensional, turbulent, boundary-layer flows of a non-reacting, two-component mixture of gases are presented in non-dimensional, Levy-Lees variables. These equations are then presented in the parabolic form for solution by the finite-difference method of Anderson and Lewis (Ref. 11). Specification of the fluid properties, eddy viscosity model, and a brief summary of the global pressure iteration scheme is included.

2.1 Governing Equations

The boundary layer equations were first non-dimensionalized as proposed by Van Dyke and then transformed using Levy-Lees variables. A reference temperature and reference viscosity were defined as

$$T^*_{ref} = U^*_\infty / C^*_p \tag{1}$$

$$\mu^*_{ref} = \mu^* (T^*_{ref}) \tag{2}$$

Using any suitable reference length L^* the Van Dyke parameter ε_{VD} became

$$\varepsilon_{VD}^2 = \mu^*_{ref} / \rho^*_\infty U^*_\infty L^* \tag{3}$$

The non-dimensional variables which were used in the present method thus become

$$x = x^*/L^* \tag{4}$$

$$y = y^*/L^* \, \varepsilon_{VD} \tag{5}$$

$$p = p^*/\rho^*_\infty U^{*2}_\infty \tag{6}$$

$$\rho = \rho^*/\rho_\infty^* \tag{7}$$

$$T = T^*/T_{ref}^* \tag{8}$$

$$U = U^*/U_\infty^* \tag{9}$$

$$v = v^*/U_\infty^* \, \varepsilon_{VD} \tag{10}$$

The resulting boundary-layer equations were transformed using the Levy-Lees variables η and ξ defined by

$$d\xi = \rho_e u_e \mu_e \, dx \tag{11}$$

and

$$d\eta = \frac{\rho u_e}{\sqrt{2\xi}} \, dy \tag{12}$$

The turbulent boundary layer equations were then expressed as:

Continuity:

$$2\xi F_\xi + V' + F = 0 \tag{13}$$

Momentum:

$$2\xi F F_\xi + VF' = \beta(\rho_e/\rho - F^2) + \left[C(1 + \varepsilon^+) F'\right]' \tag{14}$$

Energy:

$$2\xi F g_\xi + Vg' = \left[\frac{C}{Pr}(1 + \frac{Pr}{Pr_t}\varepsilon^+)g'\right]' + \left(\left[\frac{C}{Pr}(Le + \frac{Pr}{Pr_t} Le_t \, \varepsilon^+) - \frac{C}{Pr}(1 + \frac{Pr}{Pr_t}\varepsilon^+)\right] \sum_i \frac{h_i}{H_e} C_i'\right)' + \left(\left[C(1 + \varepsilon^+) - \frac{C}{Pr}(1 + \frac{Pr}{Pr_t}\varepsilon^+)\right] FF' \frac{u_e^2}{H_e}\right)' \tag{15}$$

Species:

$$2\xi FZ_{\xi} + VZ' = \left(\left[\frac{C}{Pr} \left(Le + \frac{Pr}{Pr_t} Le_t \epsilon^{+} \right) \right] Z' \right)' \tag{16}$$

where V is the transformed normal velocity component

$$V = \frac{2\xi}{\rho_e u_e \mu_e} \left[F\eta_x + \frac{(\rho v + \overline{\rho' v'})}{\sqrt{2\xi}} \right] \tag{17}$$

and where $\overline{\rho' v'}$ is the time average of the product of the fluctuating density and normal velocity. The variables F, g, Z, and C were defined as:

$$F = u/U_e \tag{18}$$

$$g = H/H_e \tag{19}$$

$$Z = C_i/C_{i,e} \tag{20}$$

and

$$C = \rho\mu/\rho_e \mu_e \tag{21}$$

Boundary conditions for the above system of equations were:
at $\eta = 0$

$$F = 0$$

$$g = H_w/H_e \qquad \text{(non-adiabatic)}$$

$$\partial g/\partial \eta = 0 \qquad \text{(adiabatic)}$$

$$V = V_w$$

$$Z = Z_w = \frac{D_{12}}{v_w}\left(\frac{\partial Z}{\partial y}\right)_w \qquad \text{(porous wall)}$$

$$\partial Z/\partial \eta = 0 \qquad \text{(slot injection)}$$

and at $\eta = \eta_e$

$$F = 1$$

$$g = 1$$

$$Z = 1$$

2.2 Parabolic Form of the Conservation Equations

Equations 13, 14, 15, and 16 when expressed in the general parabolic form become:

Momentum:

$$F'' + A_1 F' + A_2 F + A_3 + A_4 F_\xi = 0$$

$$A_1 = \frac{C'}{C} + \frac{\bar{A}_0'}{\bar{A}_0} - \frac{V}{\bar{A}_0}$$

$$A_2 = -\beta F/A_0$$

$$A_3 = \beta \rho_e/\rho A_0$$

$$A_4 = -2\xi F/A_0$$

$$A_0 = C(1 + \varepsilon^+)$$

and

$$\bar{A}_0 = A_0/C$$

Energy:

$$g'' + A_1 g' + A_2 g + A_3 + A_4 g_\xi = 0$$

where

$$A_1 = \frac{C'}{C} + \frac{\bar{A}_0'}{\bar{A}_0} - \frac{V}{\bar{A}_0}$$

$$A_2 = 0$$

$$A_3 = \left(\left[\frac{C}{Pr} (Le + \varepsilon^+ \frac{Pr}{Pr_t} Le_t) - A_0 \right] \sum_i \frac{h_i}{H_e} C_i' \right)' + \left(\left[C(1 + \varepsilon^+) - A_0 \right] FF' \frac{u_e^2}{H_e} \right)'$$

$$A_4 = -2\xi F/A_0$$

$$A_0 = \frac{C}{Pr} (1 + \frac{Pr}{Pr_t} \varepsilon^+)$$

and

$$\bar{A}_0 = A_0/C$$

Species:

$$A' + A_1 Z' + A_2 Z + A_3 + A_4 Z_\xi = 0$$

where

$$A_1 = \frac{C'}{C} + \frac{\bar{A}_0'}{\bar{A}_0} - \frac{V}{\bar{A}_0}$$

$$A_2 = 0$$

$$A_3 = 0$$

$$A_4 = -2\xi F/A_0$$

$$A_0 = \frac{C}{Pr}\left(Le + \frac{Pr}{Pr_t} Le_t\, \varepsilon^+\right)$$

and

$$\bar{A}_0 = A_0/C$$

2.3 Numerical Solution Procedure

The finite-difference scheme used to solve the transformed equations was an implicit method of the Crank-Nicolson type. The method has been used sucessfully by a number of authors including Anderson and Lewis (Ref. 11), Miner, Anderson, and Lewis (Ref. 12), Davis (Ref. 13), Blottner (Ref. 14), and Harris (Ref. 15). The equations were written in the general parabolic form

$$W'' + A_1 W' + A_2 W + A_3 + A_4 W_\xi = 0 \qquad (22)$$

where W was the dependent variable F, g, or Z and the coefficients were functions of ξ, η, W and W'. The boundary layer was considered as a grid of nodal points with a varying step size in the normal direction as shown below.

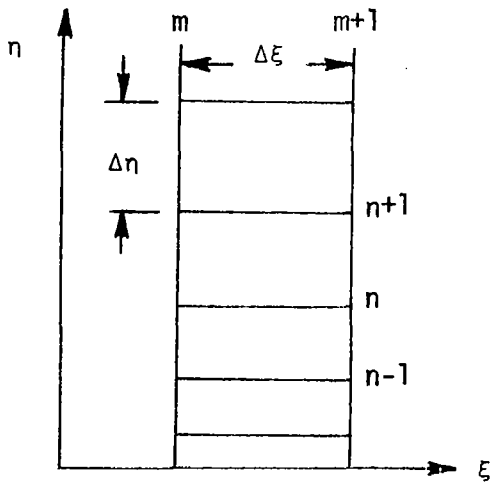

Values of the dependent variables at m + 1 were calculated across the boundary layer beginning with the boundary conditions at $\eta = \eta_e$ and using the relationship (Ref. 11)

$$W_n = E_n W_{n+1} + F_n$$

where

$$E_n = \frac{-C_n}{B_n + A_n E_{n-1}}$$

$$F_n = \frac{D_n - A_n F_{n-1}}{B_n + A_n E_{n-1}}$$

The coefficients A, B, C, and D were evaluated from the coefficients of Equation 22 and the step sizes at each grid point using the following relations:

$$A_n = \frac{2 - A_{1_n} \Delta\eta_n}{\Delta\eta_{n-1} (\Delta\eta_n + \Delta\eta_{n-1})} \tag{23}$$

$$B_n = \frac{-2 + A_{1_n} (\Delta\eta_n - \Delta\eta_{n-1})}{\Delta\eta_n \Delta\eta_{n-1}} + A_{2_n} + \frac{A_{4_n}}{\Delta\xi} \tag{24}$$

$$C_n = \frac{2 + A_{1_n} \Delta\eta_{n-1}}{\Delta\eta_n (\Delta\eta_n + \Delta\eta_{n-1})} \tag{25}$$

and

$$D_n = -A_{3_n} + \frac{A_{4_n} W_{m,n}}{\Delta\xi} \tag{26}$$

The values of E_1 and F_1 were determined by the boundary condition at $\eta = 0$. For example, when the boundary condition set $\partial W/\partial\eta$ equal to zero, E_1 became unity and F_1 became zero. In another case where W at the wall was a given value, as with porous injection or with a non-adiabatic wall, then E_1 was zero and F_1 was the value of W at the wall.

When the equations are written in the general parabolic form, they form a coupled, non-linear system which must be solved by iteration. At each value of ξ, the species, energy, and momentum conservation equations were iterated using the above procedure and the continuity equation was solved by integration of the expression

$$V = V_w - \int_0^\eta (2\xi F_\xi + F)\, d\xi \tag{27}$$

Iteration continued until Z, g, and F at each grid point across the boundary layer changed between iterations by less than the desired amount.

2.4 Fluid Properties

The fluid properties for air injected into air were obtained from the following standard relations. Density was computed from the state equation

$$\rho = pM_f/RT \tag{28}$$

and the viscosity was computed by Sutherland's formula

$$\frac{\mu}{\mu_{ref}} = \frac{T_{ref} + C^*}{T + C^*} \left[\frac{T}{T_{ref}}\right]^{3/2} \tag{29}$$

where $C^* = 110.3^\circ K$.
The transport properties were defined by setting $Pr = 0.71$, $Pr_t = 0.9$, $Le = 1.0$, and $Le_t = 1.0$.

For the case of foreign gas injection such as helium into air, thermodynamic and transport properties were supplied by the tabulated data of Jaffe, Lind, and Smith (Ref. 16). Table 1 gives the data used to compute the properties of the individual species. The species specific heat at constant pressure was $C_{pi} = 31025\ ft^2/sec^2\text{-}^\circ R$ and then enthalpy was calculated by $h_i = C_{pi}\ T\ ft^2/sec^2$. The species specific heat at constant volume was calculated from:

$$C_{vi} = C_{pi} - R/M_i$$

The mixture density was obtained as follows:

$$\rho = \frac{P}{RT}\left[\frac{M_f M_i}{C_f(M_i - M_f) + M_f}\right] \quad \text{slug/ft}^3$$

where

$$M_i = M_{He} = 4.0026$$

$$M_f = M_{Air} = 28.966$$

The enthalpy and specific heat of the mixture were calculated by the following expressions:

$$h = (1-C_f)h_i + C_f h_f$$

$$C_p = (1-C_f)C_{pi} + C_f C_{pf}$$

The mixture viscosity was calculated by Wilke's formula:

$$\mu = \frac{\mu_i}{1 + G_{if}X_f/X_i} + \frac{\mu_f}{1 + G_{fi}X_i/X_f} \tag{30}$$

where

$$X_i = (1-C_f)/M_i\left[C_f/M_f + (1-C_f)/M_i\right]$$

$$X_f = C_f/M_f\left[C_f/M_f + (1-C_f)/M_i\right]$$

and

$$G_{if} = \frac{1}{\sqrt{8}}\left(1 + \frac{M_i}{M_f}\right)^{-1/2}\left[1 + \left(\frac{\mu_i}{\mu_f}\right)^{1/2}\left(\frac{M_f}{M_i}\right)^{1/4}\right]^2$$

The mixture thermal conductivity was also calculated using Wilke's formula (30) where the species conductivity was calculated by the following expression:

$$k_i = (9C_{pi}/4C_{vi} - 5/4)C_{vi}\mu_i$$

2.5 Eddy Viscosity Model

The eddy viscosity, ε^{+*}, was computed by either a two-layer model consisting of an inner and outer region or a multi-layer model proposed by Beckwith and Bushnell (Ref. 2). Both models were based on Prandtl's mixing length concept given by

$$\varepsilon^* = \rho^* \ell^{*2} \left| \frac{\partial u^*}{\partial y^*} \right| \tag{31}$$

The two-layer model used the eddy viscosity law of Van Driest for the inner law and an outer law based on Klebanoff's modification of Clauser's law (Ref. 17) while the multi-layer model varied the definition of ℓ^* in each layer.

2.5.1 Two-Layer Model

The two-layer model separates the boundary layer into two regions, one near the wall and the other consisting of the remainder of the boundary layer. A different expression for ℓ^* in equation 31 is used in the two regions. In the present work, the expression developed by Van Driest (Ref. 18) was used in the wall region

$$\ell^* = k_1 y^* \left[1 - \exp\left(-y^+/A^+\right)\right] \tag{32}$$

where $k_1 = 0.4$

$$y^+ = y^* u_f^* / \nu^*$$

$$u_f^* = \left(\tau_w^*/\rho^*\right)^{1/2}$$

For a non-porous wall without a pressure gradient, $A^+ = 26$. For a case with mass transfer through the wall, A^+ was corrected as proposed by Cebeci (Ref. 19)

$$A^+ = 26 \exp\left(-5.9\, v_w^+\right) \tag{33}$$

where

$$v_w^+ = v_w^*/u_f^*$$

For cases with both mass transfer and pressure gradients A^+ becomes (Ref. 11)

$$A^+ = 26\left\{-\frac{p^+}{v_w^+}\left[\exp\left(11.8\, v_w^+\right) - 1\right] + \exp\left(11.8\, v_w^+\right)\right\}^{-1/2} \qquad (34)$$

where

$$p^+ = -\frac{dp_e^*}{dx^*}\, v^*/\rho^*\, (u_f^*)^3$$

The eddy viscosity law in the region near the wall becomes

$$\varepsilon^{+*} = \frac{\varepsilon^*}{\mu^*} = (k_1\, y^*)^2\left[1 - \exp\left(-Y^+/A^+\right)\right]^2 \left|\frac{\partial u^*}{\partial y^*}\right| \frac{\rho^*}{\mu^*} \qquad (35)$$

For the outer regions of the boundary layer, the eddy viscosity was based on the work of Clauser and is given by

$$\varepsilon^{+*} = k_2\, \rho^*\, u_e^*\, \delta_k^*\, \gamma/\mu^* \qquad (36)$$

where $k_2 = 0.0168$, δ_k^* is the incompressible, two-dimensional boundary-layer displacement thickness and γ is the Klebanoff intermittency factor which was approximated by

$$\gamma = \left[1 + 5.5\, (y^*/\delta^*)^6\right]^{-1} \qquad (37)$$

In the two-layer model the outer law was first used across the entire boundary layer. Then, starting at the wall, the inner law was used up through the boundary layer until the eddy viscosity from the inner law was greater than or equal to that of the outer law.

2.5.2 Multi-Layer Model

The multi-layer eddy viscosity model is due to Beckwith and Bushnell (Ref. 2) and also used by Miner and Lewis (Ref. 4). The Prandtl mixing

length concept was modified using the Van Driest damping factor to give the following expression for ε^+ in dimensional variables

$$\varepsilon^+ = \ell^2 \left[1 - \exp\left(-y^+/A^+\right)\right]^2 \left|\frac{\partial u}{\partial y}\right| \frac{\rho}{\mu} \tag{38}$$

The mixing length ℓ is then calculated in the different regions as follows:

For a fully-developed turbulent boundary layer, the flow is divided into three layers by specific values of y and the mixing length is defined in each of these layers as:

Point	y/δ	ℓ
0	0	0
1	0.1	$0.1\ K\delta$
2	0.3	$\tilde{f}\delta$

where $K = 0.4$ and $\tilde{f}$ is given by

$$\tilde{f} = 0.265 - 0.196\ H_k^* + 0.0438\ H_k^{*2}$$

where $H_k^* = \delta_k^*/\theta_k$ and θ_k is the incompressible boundary-layer momentum thickness.

For tangential slot injection, the above model was modified to consider three distinct regions or zones (Fig. 1). These zones were determined by the relative values of the mixing lengths in the slot flow region, ℓ_s, in the mixing region, ℓ_m, and in the outer region of the boundary layer, ℓ_b.

For the slot flow region the mixing length was constant and given by

$$\ell_s = a_s s/2$$

where s is the slot height and a_s is a constant. The suggested value for turbulent slot flow was $a_s = 0.14$ (Ref. 2).

In the mixing region, ℓ_m was given by

$$\ell_m = a_m \tilde{W}\ Pr_t/Le_t$$

where $\tilde{W}$ was the width of the mixing zone between the slot flow and the outer flow and a_m was a constant. The values of a_m should range from 0.05 to 0.12, with 0.09 being the recommended value (Ref. 2). The mixing zone width $\tilde{W}$ is defined by

$$\tilde{W} = y_f - y_n$$

where $y_f = y$ at $\tilde{Z} = 0.99$, $y_n = y$ at $\tilde{Z} = 0.01$ and $\tilde{Z}$ is given by

$$\tilde{Z} = (C_i - C_{i,w})/(C_{i,e} - C_{i,w})$$

The mixing length in the outer flow was defined as

$$\ell_b = \tilde{f}_s \, (\delta - y_n)$$

where $\tilde{f}_s$ was

$$\tilde{f}_s = 0.265 - 0.196 \; H^*_{k,s} + 0.0438 \; H^*_{k,s}$$

and $H^*_{k,s} = \delta^*_{k,s}/\theta_{k,s}$. The subscript s denotes that the lower limit of integration for δ^*_k and θ_k was changed from $y = 0$ to $y = y_n$ as recommended by Beckwith and Bushnell (Ref. 2).

With the above definitions of ℓ_s, ℓ_m, and ℓ_b, the three zones may be specified. Zone 1 is the initial mixing zone and is defined by the inequality

$$\ell_s \geq \ell_m < \ell_b$$

The model used in Zone 1 was a five-layer model using the following pivot points and coordinates of y and ℓ:

Point	y	ℓ
0	0	0
1	$\frac{s}{2K} a_s$	$\frac{s}{2} a_s$
2	$s\ (1 - \frac{a_s}{2K})\ \frac{\delta}{\delta_r}$	$\frac{s}{2} a_s$
3	y_m	$\frac{Pr_t}{Le_t} a_m \tilde{W}$
4	$(s + t + \frac{\tilde{f}_s \delta_o}{K})\ \frac{\delta}{\delta_r}$	$\tilde{f}_s\ (\delta - y_n)$

where s is the slot height, t is the lip thickness, $y_m = y$ at $\tilde{Z} = 0.5$, δ_o is the thickness of the boundary layer above the lip, and $\delta_r = \delta_o + s + t$.

Zone 2 was the intermediate mixing zone and used a four-layer model formed by dropping pivot point 2. This zone was defined by the inequality

$$\ell_s \leq \ell_m \leq \ell_b$$

and the pivot points and coordinates of y and ℓ are

Point	y	ℓ
0	0	0
1	$\frac{Pr_t}{Le_t} \frac{a_m}{K} \tilde{W}$	$\frac{Pr_t}{Le_t} a_m \tilde{W}$
3	y_m	$\frac{Pr_t}{Le_t} a_m \tilde{W}$
4	$(s + t + \frac{\tilde{f}_s \delta_o}{K}) \frac{\delta}{\delta r}$	$\tilde{f}_s\ (\delta - y_n)$

Zone 3 approached the equilibrium boundary-layer state and was given by

$$\ell_s \leq \ell_m \geq \ell_b$$

This zone used the three layer model and the pivot points are given by

Point	y	ℓ
0	0	0
1	0.1	$0.1\ K\delta$
4	0.3	$\tilde{f}_s\ \delta$

A schematic representation of the mixing length profiles, velocity profiles, and species concentration profiles is presented in Figure 1.

2.6 Application of the Finite-Difference Method

In order to begin the numerical solution, initial profiles for the dependent variables Z, F, and g are needed. These guesses were of the following form:

at $\eta < \eta_e$	at η_e
$F = 1 - e^{-\eta}$	$F = 1$
$F' = e^{-\eta}$	$F' = 0$
$F'' = -e^{-\eta}$	$F'' = 0$
$g = g_w + (1 - g_w)\ F$	$g = 1$
$g' = (1 - g_w)\ F'$	$g' = 0$
$g'' = (1 - g_w)\ F''$	$g'' = 0$
$Z = 1$	$Z = 1$
$Z' = 0$	$Z' = 0$
$Z'' = 0$	$Z'' = 0$

The solution of the continuity equation across the boundary layer was assumed as

$$V = V_w - \eta$$

and the temperature profile was calculated from the g profile

$$T/T_e = (1 + 1/2 \frac{U_e^2}{h_e}) g - 1/2 \frac{U_e^2}{h_e} F^2 \tag{39}$$

$$(T/T_e)' = (1 + 1/2 \frac{U_e^2}{h_e}) g' - \frac{U_e^2}{h_e} FF' \tag{40}$$

The density profile was assumed to be that of a perfect gas

$$\frac{\rho}{\rho_e} = \frac{T_e}{T}$$

and the Chapman-Rubesin Factor, $C = \rho\mu/\rho_e\mu_e$ was set to unity across the boundary layer.

Starting with the above guesses, the equations were solved to determine Z, g, and F. New values of T/T_e, $(T/T_e)'$, ρ/ρ_e, V, and C were computed where

$$V = V_w - \int_0^\eta (2\xi F_\xi + F)\, d\eta \tag{41}$$

$$C = \left[\frac{T}{T_e}\right]^{1/2} \frac{(1 + \bar{C})}{(T/T_e + \bar{C})} \qquad \text{(Sutherland's Law)}$$

where $\bar{C} = C^*/T^*_{ref}$

or

$$C = \left[T/T_e\right]^{(\omega-1)} \qquad \text{(Power Law)}$$

For tangential slot injection, the initial profiles for F, g, and Z must be supplied at the slot location. These may be obtained from experimental data or by combining the results of a flat plate, finite-difference solution with an approximation for the slot profile. In the present work, flat-plate calculations were compared with experimental Mach number profile data to match as closely as possible the boundary-layer thickness δ, the compressible displacement thickness δ^*, the momentum thickness θ, the Mach number profile and the velocity profile. The profiles which best matched these data were combined with an approximation for the slot flow and used as initial profiles at the slot location.

Boundary-layer parameters were calculated from the converged solutions of g, F, and Z at each value of ξ. The definitions used to calculate these parameters were:

Boundary-Layer Thickness:

The boundary-layer thickness, δ, was the value of y^* where $u^*/u_e^* = 0.995$ and was determined by interpolation of the F array.

Incompressible Displacement Thickness:

$$\delta_k^* = \int_0^{y_e^*} \left[1 - \frac{u^*}{U_e^*}\right] dy^* \tag{42}$$

or

$$\frac{\delta_k^*}{a^*} = \frac{\varepsilon_{VD}(2\xi)^{1/2}}{\rho_e U_e r^j} \int_0^{\eta_e} \left[\frac{\rho_e}{\rho}(1 - F)\right] d\eta \tag{43}$$

Compressible Displacement Thickness:

$$\delta^* = \int_0^{y_e^*} \left[1 - \frac{\rho^* u^*}{\rho_e^* U_e^*} \right] dy^* \tag{44}$$

or

$$\frac{\delta^*}{a^*} = \frac{\varepsilon_{VD}(2\xi)^{1/2}}{\rho_e U_e r^j} \int_0^{\eta_e} \left[\frac{\rho_e}{\rho} - F \right] d\eta \tag{45}$$

Momentum Thickness:

$$\theta^* = \int_0^{y_e^*} \frac{\rho^* u^*}{\rho_e^* U_e^*} \left[1 - \frac{u^*}{U_e^*} \right] dy^* \tag{46}$$

or

$$\frac{\theta^*}{a^*} = \frac{\varepsilon_{VD}(2\xi)^{1/2}}{\rho_e U_e r^j} \int_0^{\eta_e} F\,(1-F)\, d\eta \tag{47}$$

Skin Friction Coefficients:

$$C_{f_\infty} = \frac{2\tau_w^*}{\rho_\infty^* U_\infty^{*2}} \tag{48}$$

where $\tau_w^* = \mu_w^* \left[\frac{\partial u^*}{\partial y^*} \right]_w$

or

$$C_{f_\infty} = \frac{2\varepsilon_{VD}\, \mu_e\, C_w\, \rho_e\, U_e\, r^j}{(2\xi)^{1/2}} \left[\frac{\partial F}{\partial \eta} \right]_w \tag{49}$$

2.7 Global Pressure Interaction

The present finite-difference method contained, as an option, the iterative procedure developed by Miner and Lewis (Ref. 4) to include the effects of pressure interaction. The first boundary-layer calculation was made using the input pressure distribution $dp/dx = 0$ and calculated the displacement thickness distribution. The method then used the displacement thickness to calculate a new pressure distribution and began a new boundary-layer solution. This iteration was continued until the change in the pressure distribution between iterations was sufficiently small.

The method assumed that the flow was isentropic and that Prandtl-Meyer theory was applicable. From the displacement thickness slope, $d\delta^*/dx$, the edge Mach number was found using Prandtl-Meyer theory. Since the δ^* distribution may not be smooth, a six-point walking least squares log-log curve fit was used to calculate $d\delta^*/dx$. This curve fit provides a smoother derivative than a three or four point Lagrangian interpolating polynomial. Isentropic relations were used to calculate p/p_0 from the Mach number. Since the interaction between the pressure distribution and the displacement thickness may be rather strong, a weighting factor w was used so that

$$p_{new} = p_{old} (1 - w) + w\, p_{\delta}^*$$

where p_{new} was the pressure distribution to be used in the next iteration, p_{old} was the distribution from the last iteration, and p_{δ}^* was the distribution computed from δ^*. Suggested values of w range from 0.05 to 0.2 depending on the degree of difficulty in maintaining stability.

III. RESULTS AND DISCUSSION

The results of the present method were compared with a recent experimental study conducted by Schetz and Van Overeem (Ref. 10). The experiments were conducted in the supersonic wind tunnel at Virginia Polytechnic Institute and State University. Air was injected through a 0.635 cm (0.25 in.) slot and/or a 3.81 cm (1.5 in.) porous plate. The width of the wind tunnel test section was 22.86 cm (9.0 in.) which gave for the slot an injection area of 14.52 cm^2 (0.01563 $ft.^2$) and for the porous plate, an area of 82.26 cm^2 (0.08854 $ft.^2$). Since combinations of slot and porous geometries were considered, the results were presented in terms of the total mass flow $\dot{m} = \rho_j u_j A_j$ and non-dimensionalized by a reference freestream value defined as $\rho_\infty u_\infty$ (1 $ft.^2$). These experiments were conducted at $M_\infty = 2.9$, with a stagnation temperature of 294°K, and a stagnation pressure of 6.803 atmospheres. Pitot pressure profiles, wall pressure, and wall shear stress data were taken throughout a range of mass injection rates. The nozzle was modified so that the streamline along the axis of the two-dimensional, symmetric nozzle was replaced by a solid surface (see Fig. 2a). Since the lower portion of the modified nozzle was a flat surface, a flat-plate geometry was used in the present method to simulate the experimental conditions. The use of this geometry caused some problems in determining the initial value of ξ, the streamwise coordinate. The nozzle boundary layer begins forming somewhere upstream of the curved portion of the converging section of the nozzle while the flat-plate boundary layer is assumed to begin at the leading edge of a constant pressure flat plate. Thus the virtual flat-plate length had to be determined to best simulate the boundary layer on the nozzle wall. Experimental pitot pressure profiles, taken at the slot location, were compared with calculations of the flow over a flat plate. The predicted profiles best matched the measured profiles at a distance of 53.34 cm (21.0 in.) downstream of the leading edge. Figure 3 shows good agreement between the flat-plate prediction and the experiment at

this location. The value of ξ = 7.8975 at 53.34 cm was used as the initial value of ξ for the mass injection study.

Initial profiles were taken from the experimental data of Ref. 10 at the slot location. Pitot profiles were measured at the slot and used to obtain Mach number profiles, assuming a constant static pressure. By assuming a constant total enthalpy profile (H/H_e = 1.0), initial velocity profiles were calculated from the Mach numbers. The initial air species profile for helium injection was set to unity above the slot lip and to zero below the lip. For the cases using air injection the species profile was set to unity across the boundary layer.

Flat-Plate Results

The above determined initial profiles were used to simulate a boundary-layer flow over a flat plate. The predicted skin friction was 40% higher than measured by the floating-element balance. No Preston tube measurements were obtained on the solid flat-plate; however, extrapolation of the Preston data to $\dot{m}$ = 0 presented in Fig. 9, gave considerably higher values of wall shear than were measured by the floating-element balance. To help resolve these differences, the results were compared with previous investigations. Figure 4 compares the skin friction under the present conditions with data by Coles (Ref. 20) and the numerical results of Anderson and Lewis (Ref. 11). The present results are in excellent agreement with Anderson and Lewis and fall between Cole's Case 26 and Case 20. The extrapolated Preston tube value also agrees well with the present method but the balance data on both the solid plate and the porous plate with $\dot{m}$ = 0 were low. Since the skin-friction distribution was not measured with either the balance or the Preston tube, it was impossible to resolve the differences between the balance data and the present prediction. Figure 5 shows the measured velocity profile at the slot location in law-of-the-wall coordinates. Again the numerical results and extrapolated Preston tube data are in good agreement while the balance data are below the prediction.

Without skin-friction distributions it was impossible to determine whether or not the balance and Preston tube data show the same flat-plate trends.

Figures 6-8 show the Mach number profiles at three locations downstream of the slot.

Normal Injection Through a Porous Wall

The first mass transfer geometry considered was a porous wall. Porous-wall injection caused a large reduction in the skin friction, but the effectiveness of the porous wall injection was limited by boundary-layer separation. Figure 9 presents the skin-friction variation as a function of the mass transfer rate. The balance and Preston tube data again do not agree. At high injection rates, the balance data were slightly lower than the Preston tube data but had a similar slope. At low injection rates, the agreement was poorer. The limited Preston tube data indicated a much more rapid reduction in skin friction with mass transfer than the balance data, and the Preston tube predicted a higher skin-friction at $\dot{m} = 0$. Differences in the two measurement techniques create some question as to the effectiveness of normal injection. The Preston tube data show the porous wall was the most effective geometry per unit mass in reducing skin friction. The balance data show it was the least effective. More experimental data are needed to determine conclusively the effectiveness of the porous wall. The numerical study showed very good agreement with the Preston tube data and predicted boundary-layer separation over the porous plate when the mass-transfer rate was greater than $\dot{m}/\rho_\infty u_\infty$ (1) = 0.0016 or $\rho_w v_w/\rho_\infty u_\infty$ = 0.01807. This separation would account for the sudden loss in effectiveness evident in the Preston tube data. The balance data show the porous-wall technique suffered from a roughness-induced increase in skin friction, but no Preston tube data were available to confirm this increase. Since the balance did measure lower skin-friction values on the flat plate, this apparent increase should be confirmed by additional experimental data. It is probable

that the balance was more sensitive to roughness effects since it was flush with the wall and completely enveloped by the sublayer. The Preston tube, on the other hand, could not be placed on the surface due to the finite thickness of the tube walls and may be above the sublayer which was most affected by the roughness. More Preston tube and balance data are needed to better determine the effects of roughness of the porous surface on the skin friction.

Calculations were also made which included the effects of pressure interaction. The pressure distribution resulted in higher skin-friction values than did the case with a constant edge pressure. As the mass injection rate increased, the effects of pressure interaction increased because the predicted pressure gradients became stronger over the porous section (see Fig. 10). These increased pressure gradients also caused the boundary layer to separate at lower mass injection rates than the cases without pressure interaction. Mach number profile comparisons at two different injection rates are presented in Figs. 11-16. At the lower injection rate, the agreement with experimental measurements was excellent and pressure interaction had very little effect. At the higher injection rate, the agreement was rather poor with the predicted Mach numbers being as much as 20% lower than the experimental data. Pressure interaction solutions showed better agreement but were still as much as 10% too low. As the external stream flowed over the porous plate, normal injection caused a thickening of the boundary layer. Downstream of the porous section, the boundary layer became thinner after the normal injection stopped. In the low injection case, the thickening of the boundary layer was not very severe and the flow recovered quickly thus giving good agreement with the profiles taken downstream of the porous section. At the high injection rate, however, the boundary layer became much thicker and could not adjust as quickly; thus the present method predicted a much thicker boundary layer downstream of the porous wall. The pressure gradient behind the porous section was favorable and resulted in better agreement with the experimental profiles.

Pitot pressure profiles for the first two stations at both injection rates are presented in Figs. 17-20. The results were similar to those of the Mach number profiles except near the outer edge of the boundary layer at station one. Here the experimental data do not asymptotically approach unity at the edge. This condition was caused by shock waves generated at the junction of the injection box and the test section wall as shown by the Schlieren photographs in Ref. 10. At station two, the probes were completely behind these waves and the profiles did not show a jump near the outer edge of the boundary layer.

Tangential Injection Through a Slot

The second injection geometry considered was a tangential slot. In this part of the study, both eddy viscosity models were used and a foreign gas injectant was briefly considered. Figure 21 presents the skin-friction variation with the mass-transfer rate. The balance data were again lower than the Preston tube data, but the experimental results did show the same trends. The Van Driest-Clauser eddy viscosity model predicted a skin-friction distribution about 30% higher than did the Beckwith-Bushnell model. The difference is due to the differences in the velocity profiles caused by changing eddy viscosity models (see Fig. 28). The Beckwith-Bushnell model agreed well with the Preston tube data. Pressure interaction did not have the effect on slot injection that it had on the porous wall geometry since the pressure gradients were weaker as shown in Fig. 22. The presence of the step in the wall caused a 12% reduction in the skin friction from the flat-plate value as shown in Fig. 4. The skin friction continued to decrease with an increase in mass transfer until the matched pressure injection condition was reached near $\dot{m}/\rho_\infty u_\infty$ (1) = 0.0016. This mass flow rate corresponds to $\lambda = \rho_j u_j/\rho_\infty u_\infty = 0.1024$, and the slot Mach number was approximately 0.6. As the mass flow rate continued to increase, the turbulence level in the slot became high enough to cause an increase in the wall shear stress.

Calculations were made to compare the wall pressure distribution with the experimental data. For this part of the study, the numerical method used the same edge pressure as the experiment, $p_e/p_0 = 0.031$. This resulted in a freestream Mach number of 2.91 which was slightly higher than the 2.8 used in the skin-friction study. Figure 22 shows the predicted wall pressure distribution was in reasonable agreement with the measured values.

A special case using helium as the injectant was briefly considered. Figure 23 shows the skin-friction variation with mass transfer using the two-layer eddy viscosity model. The agreement with the experimental data was good. Comparison of Figs. 21 and 23 shows that helium was more effective in reducing the skin friction than air. No other experimental data are available from the helium injection study.

Comparisons of the predicted and experimental Mach number profiles for the slot configuration are made in Figs. 24-26 for the case of $\dot{m}/\rho_\infty u_\infty$ (1) = 0.00072. Figures 24-26 compare the profiles from both eddy viscosity models with the experimental results at $\dot{m}/\rho_\infty u_\infty$ (1) = 0.00072. At station 1, the Van Driest-Clauser model gave excellent agreement in the outer region of the boundary layer but did not agree well near the wall. The Beckwith-Bushnell model gave better agreement throughout the entire boundary layer especially near the wall. Pressure interaction had little effect on the multi-layer model but resulted in much better agreement when the two-layer model was used. Figure 22 shows the pressure was recompressed to the freestream value more quickly using the Van Driest model than when using multi-layer model. The pressure gradient at the first probe station was larger using the Van Driest model and thus had a greater effect on the solution. At station 2, the Beckwith-Bushnell model again agreed better near the wall than did the two-layer model. Here pressure interaction had a greater effect on the multi-layer model because the Van Driest model had recovered to the freestream pressure and experienced a small pressure gradient. A weak adverse

pressure gradient existed downstream of the slot as the flow first over-expanded around the step and then was recompressed to the freestream pressure causing a thicker boundary layer to be predicted by the pressure interaction solution. Profiles at the third station showed the two-layer model results were in better agreement with the data than the multi-layer model. The pitot profiles presented in Figs. 27-29 show the same agreement as the Mach number profiles.

In general, the Beckwith-Bushnell eddy viscosity model gave better agreement near the slot, while further downstream, the Van Driest-Clauser model more closely matched the experimental data. The present method underpredicted the Mach number profile considerably. This was due to the low mass injection rate which corresponds to $\lambda = 0.046$ and which was about 40% lower than the low pressure injection rate used in Refs. 5 and 6. Miner and Lewis (Ref. 6) found the present method overpredicted the Mach number profiles at matched pressure injection but gave good agreement at the low pressure rate. The present work shows that at even lower injection rates the method underpredicts the Mach number profiles.

Combined Slot and Porous Wall Injection

A combination of the two previous geometries was considered in the third part of this study. Air was injected through the slot and porous plate at varying mass-flow rates. Calculations predicted separation would occur over the porous section when more than 30% of the total mass flow was injected through the porous wall. Figure 30 compares the skin-friction reduction using both eddy viscosity models for the cases of 100% slot injection and 75% slot/25% porous injection. The Beckwith-Bushnell model predicted lower skin-friction than the Van Driest-Clauser model because of differences in the velocity profiles near the slot as seen in Figure 32.

One would expect combined injection to show characteristics of both the porous wall and slot injection geometries. Normal injection through

a porous wall decreased the skin friction markedly but separation occurred at mass flow rates of $\dot{m}/\rho_\infty u_\infty$ (1) = 0.0017. Slot injection also reduced the skin friction but reached a mass flow rate where the skin friction reached a minimum and then began to increase. The calculations for combined injection did indeed show characteristics of both geometries. At low mass injection rates, the porous plate reduced even further the skin friction downstream of the slot, but at the higher injection rates, the slot turbulence level increased causing the skin friction to increase. The most important effect of downstream normal injection was the decrease in the minimum skin friction attainable. The Beckwith-Bushnell model predicted a 50% lower skin friction with the 75% slot/25% porous geometry than with the slot-only case. The minimum was shifted to higher injection rates for combined injection because only a portion of the total mass flow was transferred through the slot, and thus the slot Mach number was lower even though the total mass flow was the same.

Pressure interaction had little effect on the slot flow but increased considerably the skin friction on the porous wall. A similar result was evident in the combined slot/porous injection case. At low injection rates, where the normal injection was most effective, pressure interaction solutions predicted higher skin-friction values. At higher rates, where the slot injection effects were stronger, pressure interaction caused only small differences.

Insufficient experimental data were available to validate the present predictions and most of those were from the skin-friction balance. The presence of the porous section again caused a large increase in the shear stress measured by the balance. At a mass flow of $\dot{m}/\rho_\infty u_\infty$ (1) = 0.00074, the balance measured a 76% increase over the slot-only configuration. As mentioned above, the balance was probably more sensitive to surface roughness than was the Preston tube, but it remains to be determined if roughness alone could account for such a large change. The Preston tube

measurements were not complete enough to determine whether or not surface roughness affected the Preston tube. The differences between the prediction and experiment could not be resolved with the limited experimental data available. It is impossible to completely validate the predictions from the numerical method until more experimental data are available.

Predictions of the wall pressure distribution again showed only reasonable agreement with the experimental data as shown in Fig. 31. Mach number profiles shown in Figs. 32-34 and pitot pressure profiles shown in Figs. 35-37 were similar to results for the slot geometry. The Beckwith-Bushnell eddy viscosity model again showed better agreement near the slot than did the Van Driest-Clauser eddy viscosity model. Further downstream, however, the two-layer model more closely matched the experimental data than did the multi-layer model, but both eddy viscosity laws predicted a thicker boundary layer than was measured. This was caused by the high percentage of the flow entering through the porous wall. When more than 30% of the flow was injected through the wall, separation was predicted to occur over the porous section. The 70% slot/30% porous injection case was very close to this limit, and therefore the flow was near blow-off over the plate. The flow did not recover quickly downstream of the porous wall, and thicker profiles were predicted at the measurement stations.

Pressure interaction solutions using the two different eddy viscosity models showed completely reversed trends. Using the Van Driest model, pressure interaction caused a thicker boundary layer, but using the Beckwith-Bushnell model, a thinner boundary layer was predicted. Figure 31 shows the edge pressure was actually decreasing behind the porous plate using the multi-layer model. This favorable pressure gradient caused the thinner boundary layer while the solution using the Van Driest model was subjected to an adverse pressure gradient which thickened the boundary layer.

Figure 38 shows a comparison of the skin-friction variation with the mass flow rate for the three geometries considered. According to the present predictions, the porous wall geometry provided the greatest reduction in skin friction per unit mass of injectant but was limited to low injection rates by boundary-layer separation. Tangential slot and combined injection geometries both produced a reduction of wall shear stress due to the presence of the step in the wall. Slot injection decreased the skin friction as the mass flow increased until the turbulence level became great enough to cause an increase in the wall shear stress. The combined injection model predicted even lower skin friction at low flow rates than did the slot geometry. The greatest effect of the combined injection was to reduce the minimum in skin friction at the matched pressure slot injection condition caused by injecting a portion of the flow through the wall. This delay allowed the slot/porous injection to produce a lower minimum skin friction before the slot turbulence became large enough to increase the wall shear stress. The numerical results and Preston tube data show normal injection was the most effective in reducing skin friction per unit mass injected. Schetz and Van Overeem (Ref. 10) concluded that the slot injection was the most effective based on the balance data. The reason for this contradiction was the balance data indicated normal injection to be far less effective in reducing skin friction than the Preston tube data or numerical results predicted. More data are needed for comparison to resolve the differences between the Preston tube, floating-element balance, and the present predictions.

IV. CONCLUSIONS

In the present study a finite-difference method was used to predict skin-friction reduction for porous wall and/or slot injection geometries. A comparison of the three injection geometries showed that normal injection provided the greatest reduction in skin friction per unit mass of injectant but was limited by boundary-layer separation. The tangential slot and combined injection geometries both produced a lower skin friction at $\dot{m} = 0$ due to the step in the wall. As the mass injection through the slot increased, the skin friction decreased until the mass flow rate became so large that the turbulence level caused the skin friction to increase.

Combined injection offered some improvement over the slot geometry at low mass injection and showed considerable promise at the higher injection rates. With a portion of the mass flow coming through the porous wall, the increase in slot turbulence and skin friction was delayed. This situation resulted in predicting a much lower skin friction before the slot turbulence became great enough to increase the skin friction. The numerical calculations predicted separation would occur over the porous section of the wall when more than 30% of the total mass flow was injected through the porous wall. Comparisons of the predictions with the limited Preston tube data were good while comparisons with the balance data were poorer. Differences exist in the data from the Preston tube and the floating-element balance. First of all, the balance data were lower than previous zero pressure-gradient flat-plate investigations at similar Mach numbers while no Preston tube measurements were available from Schetz and Van Overeem. The balance also measured an increase in skin friction over the flat plate when the porous section was added. This increase was attributed to surface roughness by Schetz and Van Overeem (Ref. 10) while no Preston tube data were taken for comparison. The

balance data indicate that normal injection was not the most effective injection geometry, whereas the limited Preston tube data show just the opposite. For the combined slot/porous geometry, the balance measured a large increase in skin friction over the slot-only case, but the Preston tube data showed no such increase. More experimental data are needed to resolve the differences in the two measurement techniques and to determine the effects of surface roughness on the skin friction.

Mach number profile comparisons showed good to excellent agreement with the experimental data at low injection rates. At the higher mass-transfer rates, the present calculations predicted a boundary-layer thickness that was almost 25% greater than the measured value. For the slot and combined geometries, the Beckwith-Bushnell eddy viscosity model gave better agreement near the slot than did the Van Driest-Clauser model. Further downstream, the two-layer model more closely matched the experimental data than did the multi-layer model.

Pressure interaction caused a substantial increase in the porous plate skin friction but made little difference in the slot injection case. With combined injection, pressure interaction increased wall shear at low mass flow rates but had little effect at the higher rates. The global pressure interaction scheme also gave a reasonable prediction of the wall pressure distribution. On the porous plate, the favorable pressure gradient caused a thinner boundary layer in the pressure interaction solutions. For the slot injection a weak adverse pressure gradient resulted in a thicker boundary layer.

REFERENCES

1. Patankar, S. V., and Spalding, D. B., Heat and Mass Transfer in Boundary Layers, C. R. C. Press, 1967.

2. Beckwith, I. E., and Bushnell, D. M., "Calculation by a Finite-Difference Method of Supersonic Turbulent Boundary Layers with Tangential Slot Injection," NASA TN D-6221, 1971.

3. Bushnell, D. M., "Calculation of Relaxing Turbulent Boundary Layers Downstream of Tangential Slot Injection," J. Spacecraft, Vol. 8, No. 5, May 1971, pp. 550-551.

4. Miner, E. W., and Lewis, C. H., "A Finite-Difference Method for Predicting Supersonic Turbulent Boundary-Layer Flows with Tangential Slot Injection," NASA CR-2124, 1972.

5. Kenworthy, M. A., and Schetz, J. A., "An Experimental Study of Slot Injection into a Supersonic Stream," NASA CR-2128, January 1973.

6. Miner, E. W., and Lewis, C. H., "Supersonic Turbulent Boundary-Layer Flows with Tangential Slot Injection," AIAA Paper No. 73-696, July 1973.

7. McRee, D. J., Peterson, J. B., and Braslow, A. L., "Effect of Air Injection Through a Porous Surface and Through Slots on Turbulent Skin Friction at Mach 3," NASA TN D-2427, August 1964.

8. Cary, A. M., Jr., and Hefner, J. N., "Film-Cooling Effectiveness in Hypersonic Turbulent Flow," AIAA Journal, Vol. 8, No. 11, November 1970, pp. 2090-2091.

9. Cary, A. M., Jr., and Hefner, J. N., "An Investigation of Film-Cooling Effectiveness and Skin Friction in Hypersonic Turbulent Flow," AIAA Paper No. 71-599, June 1971.

10. Schetz, J. A., and Van Overeem, J., "Skin Friction Reduction in Supersonic Flow by Injection Through Slots, Porous Sections, and Combinations of the Two," NASA CR-2491, 1975.

11. Anderson, E. C., and Lewis, C. H., "Laminar or Turbulent Boundary-Layer Flows of Perfect Gases or Reacting Gas Mixtures in Chemical Equilibrium," NASA CR-1893, 1971

12. Miner, E. W., Anderson, E. C., and Lewis, C. H., "A Computer Program for Two-Dimensional and Axisymmetric Nonreacting Perfect Gas and Equilibrium Chemically Reacting Laminar, Transitional and/or Turbulent Boundary-Layer Flows," College of Engineering Report VPI-E-71-8, VPI&SU, Blacksburg, Virginia, May 1971. (Available as NASA CR-132601.)

13. Davis, R. T., "The Hypersonic Fully Viscous Shock-Layer Problem," Sandia Laboratories Report SC-RR-68-840, 1968.

14. Blottner, J. G., "Non-Equilibrium Laminar Boundary-Layer Flow of Ionized Air," General Electric Report R64SD56. Also AIAA Journal, Vol. 2, No. 11, November 1964, pp. 1921-1927.

15. Harris, J. E., "Numerical Solution of the Compressible Laminar, Transitional, and Turbulent Boundary Layer Equations," PhD Dissertation, VPI&SU, Blacksburg, Virginia, 1970.

16. Jaffe, N. A., Lind, R. C., and Smith, A. M. O., "Solution to the Binary Diffusion Laminar Boundary Layer Equations Including the Effect of Second-Order Transverse Curvature," AIAA J., vol. 5, no. 9, Sept, 1967, pp. 1563-1569.

17. Klebanoff, P. S., "Characteristics of Turbulence in a Boundary Layer with Zero Pressure Gradient," NASA TN-3178, 1954.

18. Van Driest, E. R., "On Turbulent Flow Near a Wall," J. Aero. Sci., Vol. 23, No. 11, November 1956, pp. 1008-1011, 1036.

19. Cebeci, T., "Behavior of Turbulent Flow Near a Porous Wall with Pressure Gradient," AIAA Journal, Vol. 8, No. 2, December 1970, pp. 2152-2156.

20. Coles, D., "Measurements of Turbulent Friction on a Smooth Flat Plate in Supersonic Flow," J. Aero. Sci., Vol. 21, No. 7, July 1954, pp. 433-448.

Table 1. Thermodynamic and Transport Property Data for Helium Injection

Air Specific Heat at Constant Pressure

$$C_p = A + BT + CT^2 + DT^3 + ET^4 + FT^5 \quad ft^2/sec^2 - {}^\circ R$$

$$0\ {}^\circ R \leq T \leq 2000\ {}^\circ R$$

$A = 6.03517\ (10^{3})$	$C = -7.30226\ (10^{-4})$	$E = -9.76574\ (10^{-10})$
$B = -9.45091\ (10^{-4})$	$D = 1.73227\ (10^{-6})$	$F = 1.74651\ (10^{-13})$

Air Static Enthalpy

$$h_j = AT + BT^2 + CT^3 + DT^4 + ET^5 + FT^6 \quad ft^2/sec^2$$

$$0\ {}^\circ R \leq T \leq 2000\ {}^\circ R$$

$A = 6.03517\ (10^{3})$	$C = -2.43408\ (10^{-4})$	$E = -1.95314\ (10^{-10})$
$B = -4.72545\ (10^{-4})$	$D = 4.33069\ (10^{-7})$	$F = 2.91086\ (10^{-14})$

Viscosity

$$\mu_j \times 10^7 = A + BT + CT^2 + DT^3 + ET^4 + FT^5 \quad lb_f - sec/ft^2$$

$$90\ {}^\circ R \leq T \leq 6300\ {}^\circ R$$

Air

$A = -1.93368\ (10^{-2})$	$C = -3.9185\ (10^{-6})$	$E = -1.64934\ (10^{-13})$
$B = 8.93259\ (10^{-3})$	$D = 1.17285\ (10^{-9})$	$F = 8.75154\ (10^{-18})$

Helium

$A = 5.50269\ (10^{-1})$	$C = -2.21781\ (10^{-6})$	$E = -1.80635\ (10^{-14})$
$B = 7.94717\ (10^{-3})$	$D = 4.04477\ (10^{-10})$	$F = -1.01127\ (10^{-18})$

Binary Diffusion Coefficient

$$p\ D_{ij} = A + BT + CT^2 + DT^3 + ET^4 + FT^5 \quad lb_f/sec$$

$$90\ {}^\circ R \leq T \leq 6300\ {}^\circ R$$

Helium

$A = -9.75983\ (10^{-2})$	$C = 3.99118\ (10^{-6})$	$E = 4.70538\ (10^{-14})$
$B = 1.43997\ (10^{-3})$	$D = -4.05169\ (10^{-10})$	$F = -2.35942\ (10^{-18})$

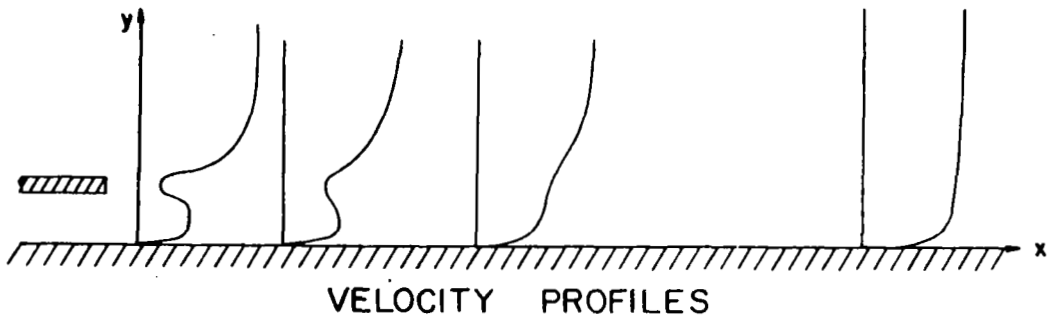

VELOCITY PROFILES

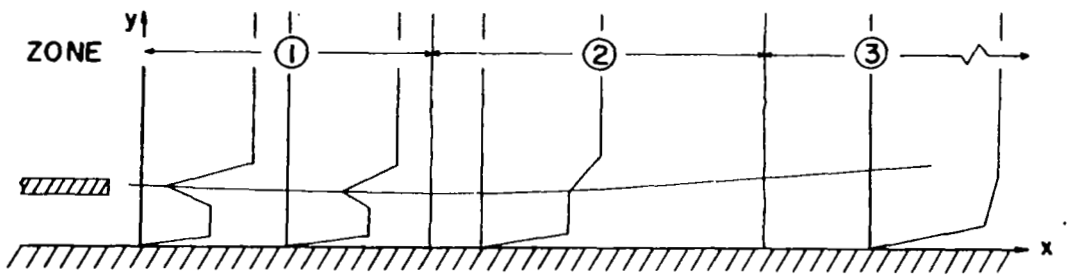

MIXING LENGTH PROFILES

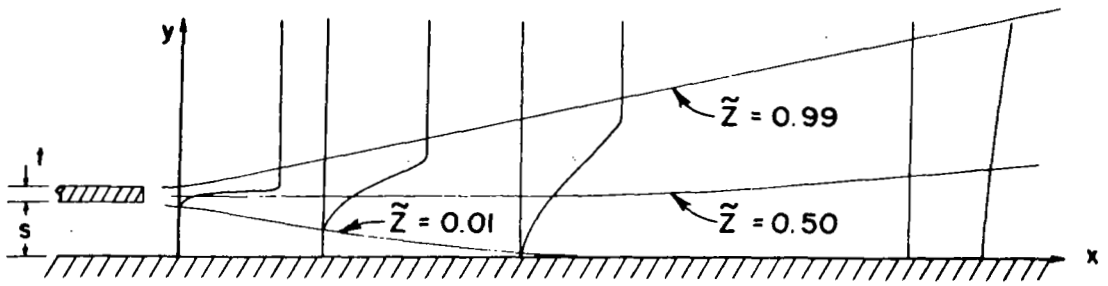

SPECIES CONCENTRATION PROFILES

Figure 1: Schematic of Slot Injection Flow Field

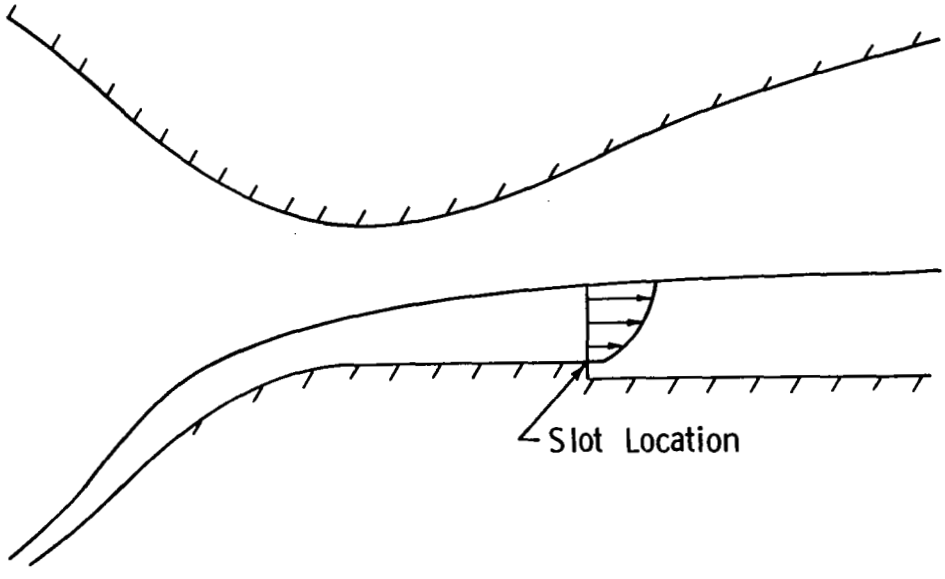

a) EXPERIMENTAL CASE

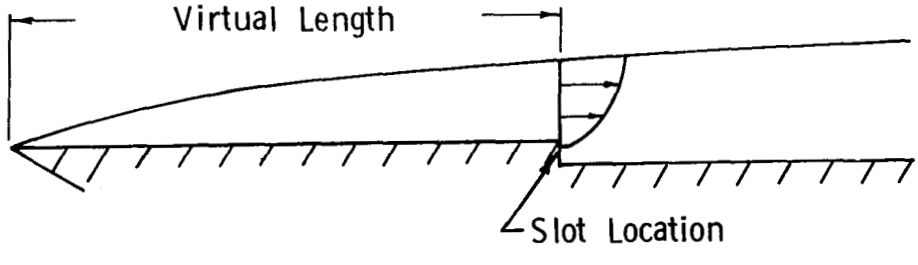

b) NUMERICAL STUDY

Figure 2: Schematic of Experimental Nozzle and Model for Numerical Calculations

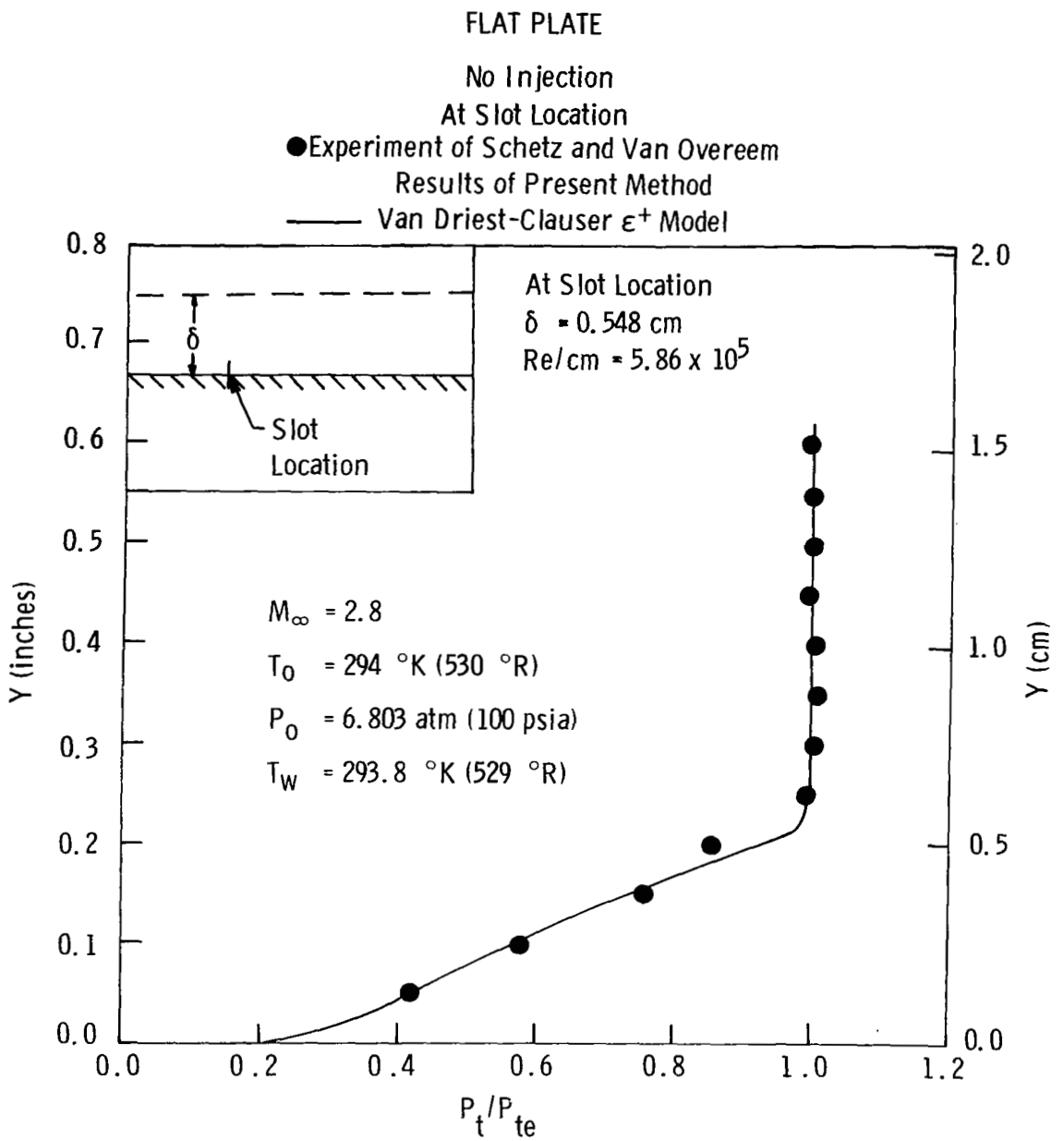

Figure 3: Flat Plate Pitot Pressure Profiles, x = 0.0 cm

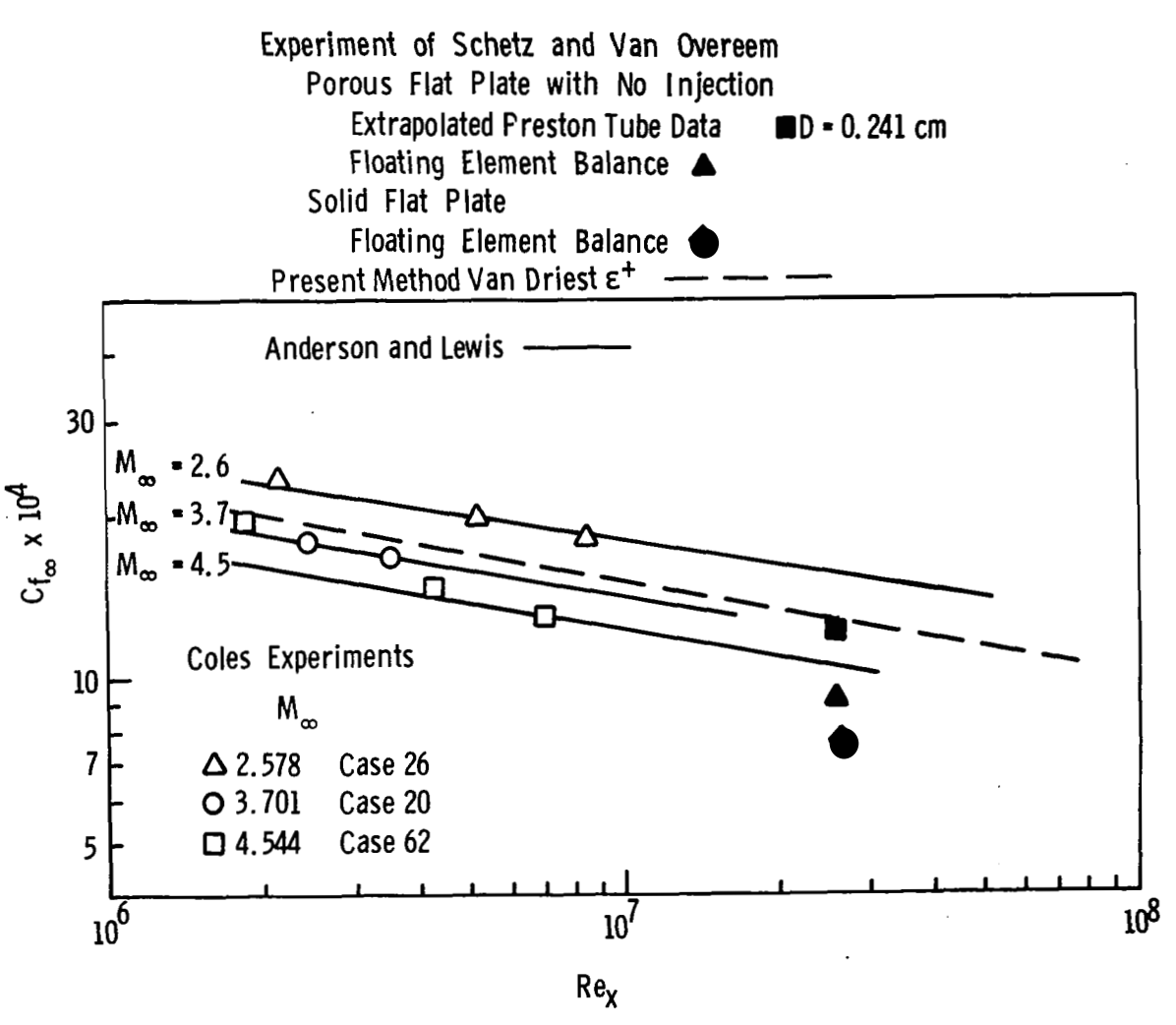

Figure 4: Flat Plate Skin Friction

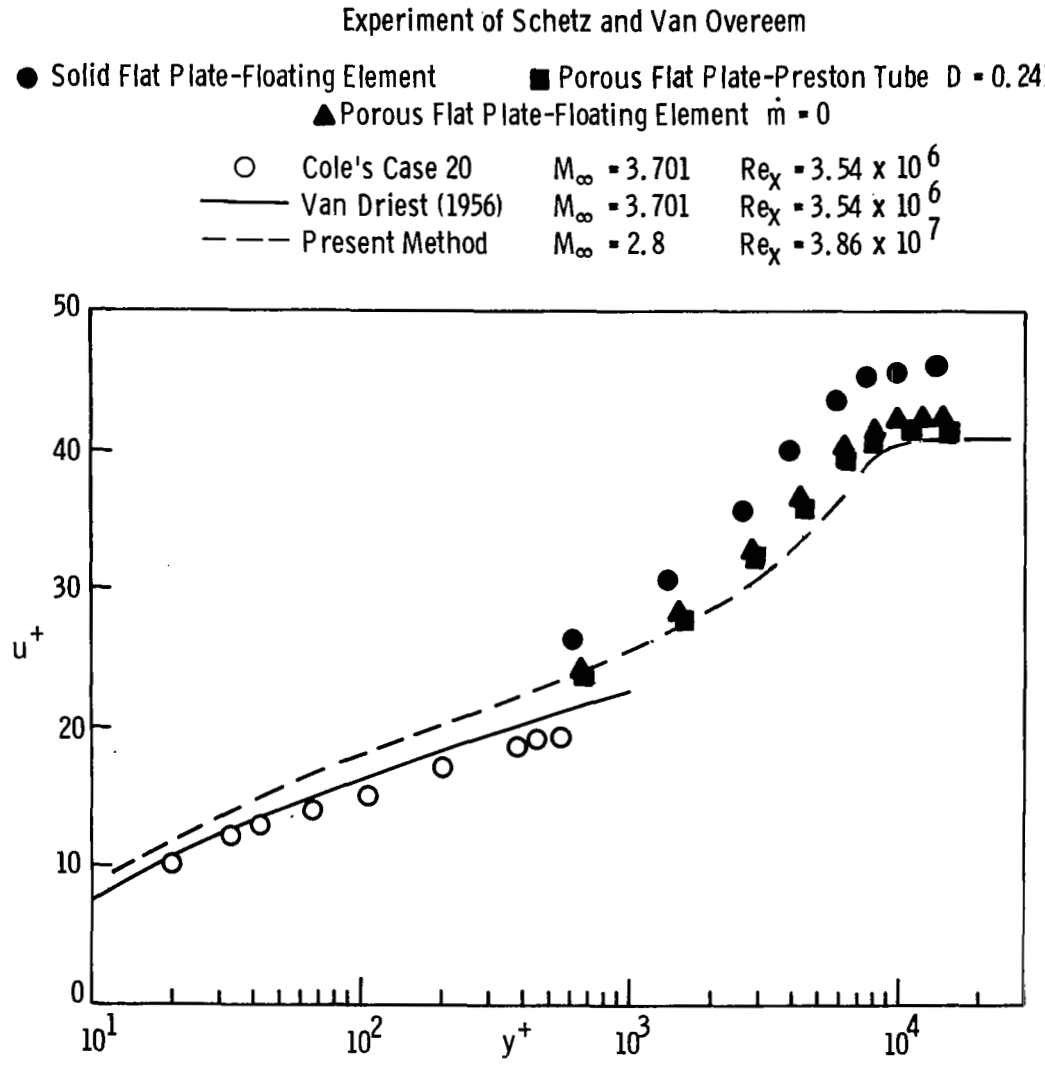

Figure 5: Velocity Profiles at Slot Location, Law of the Wall Variables

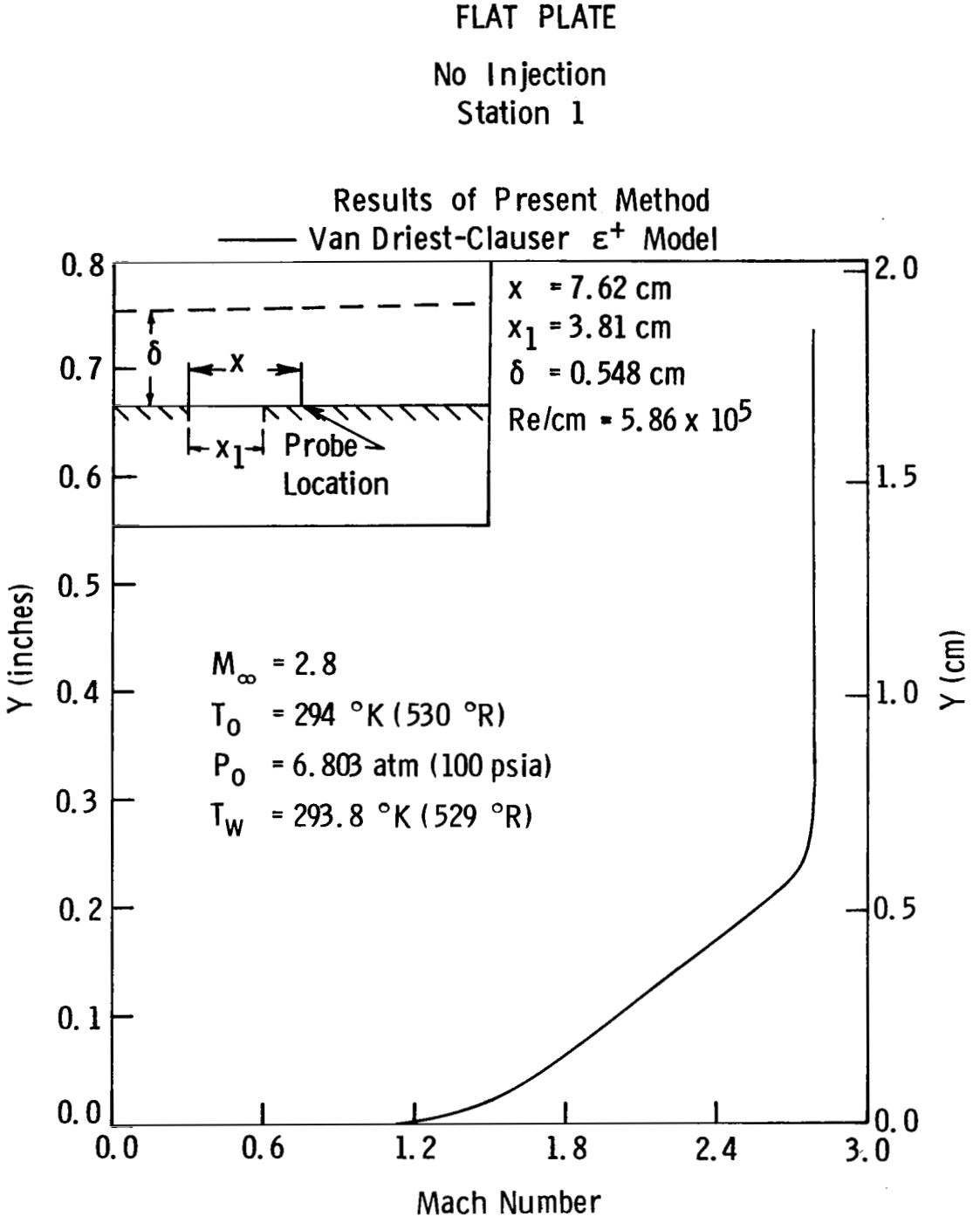

Figure 6: Flat Plate Mach Profiles, Station 1

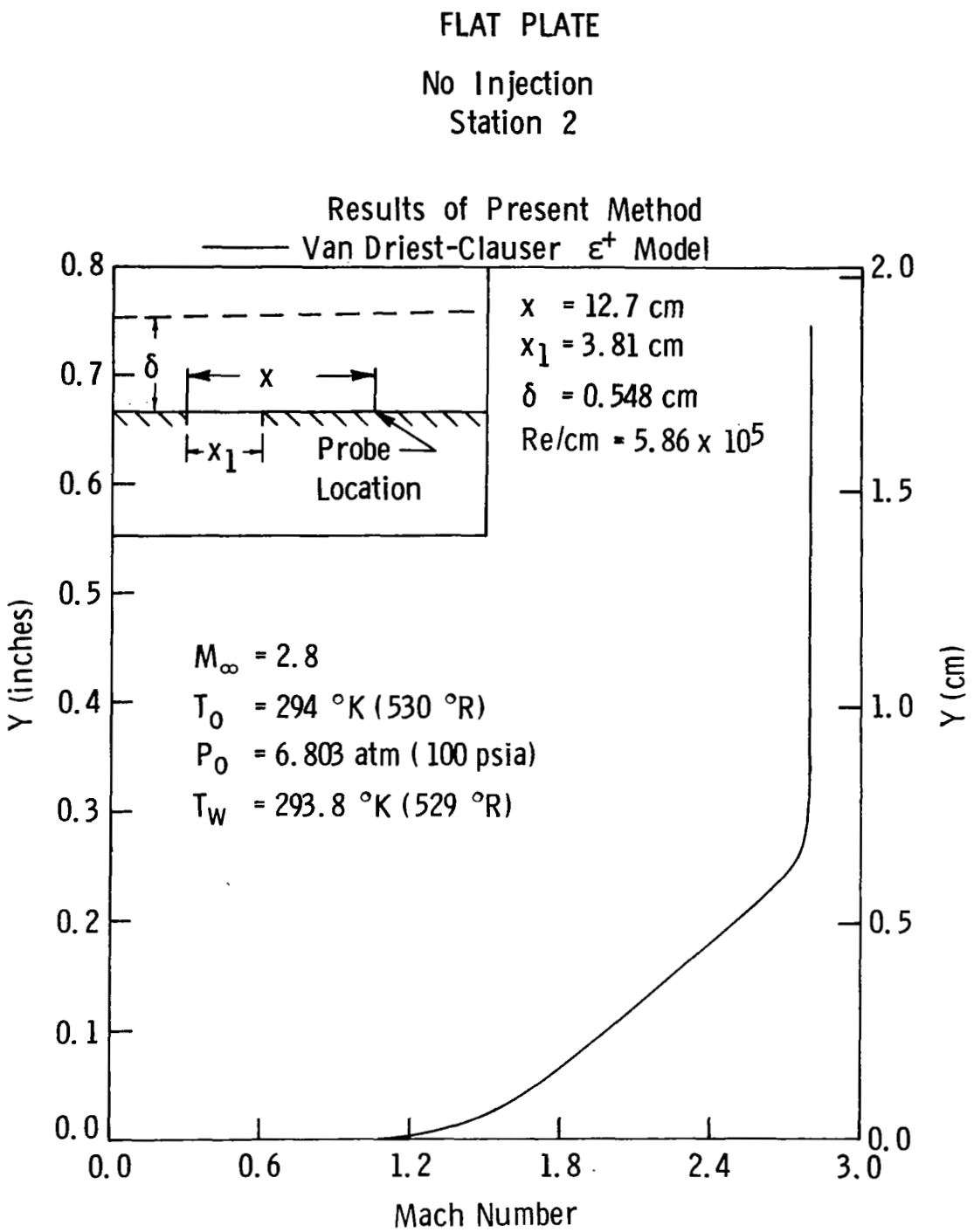

Figure 7: Flat Plate Mach Profiles, Station 2

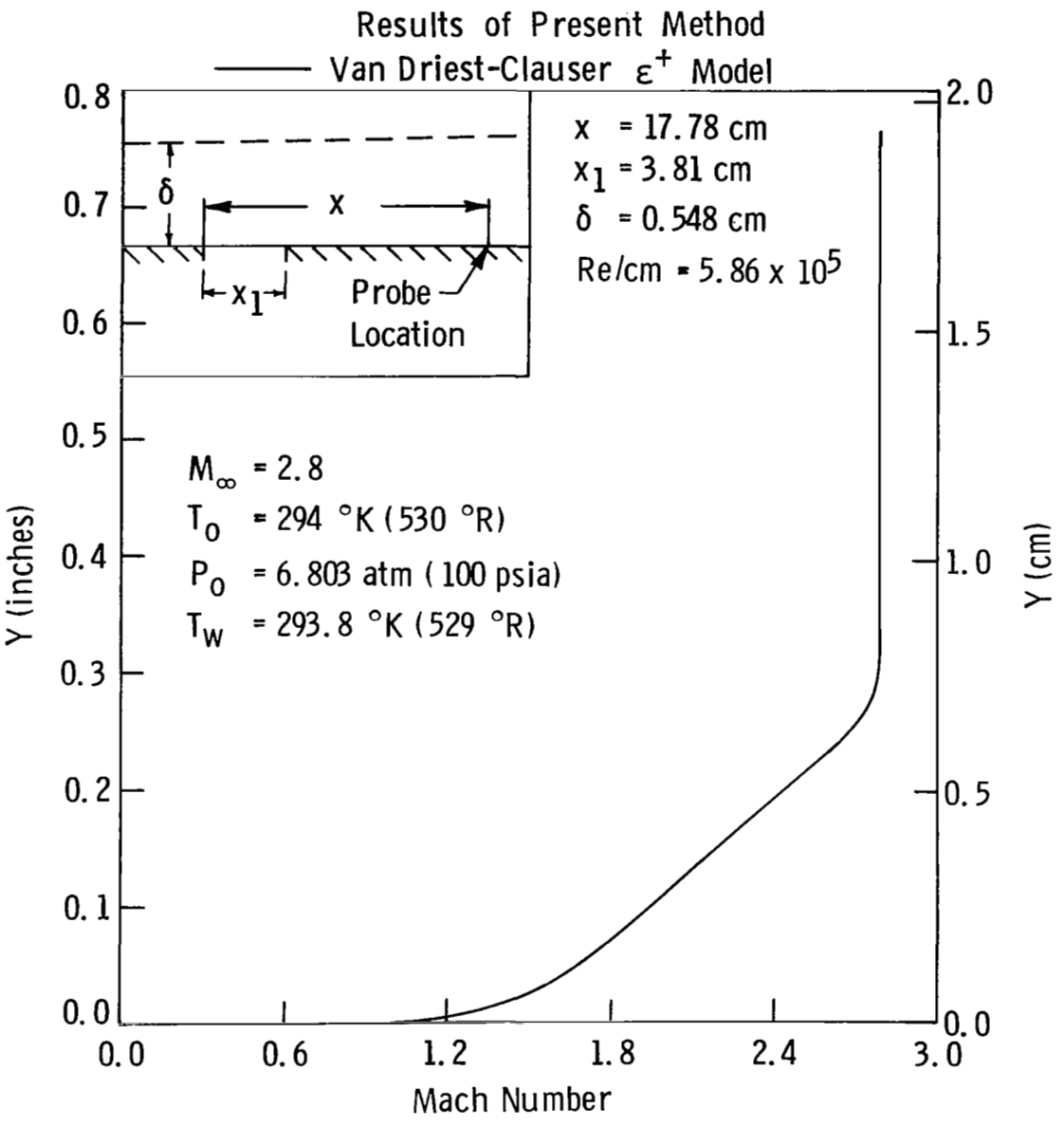

Figure 8: Flat Plate Mach Profiles, Station 3

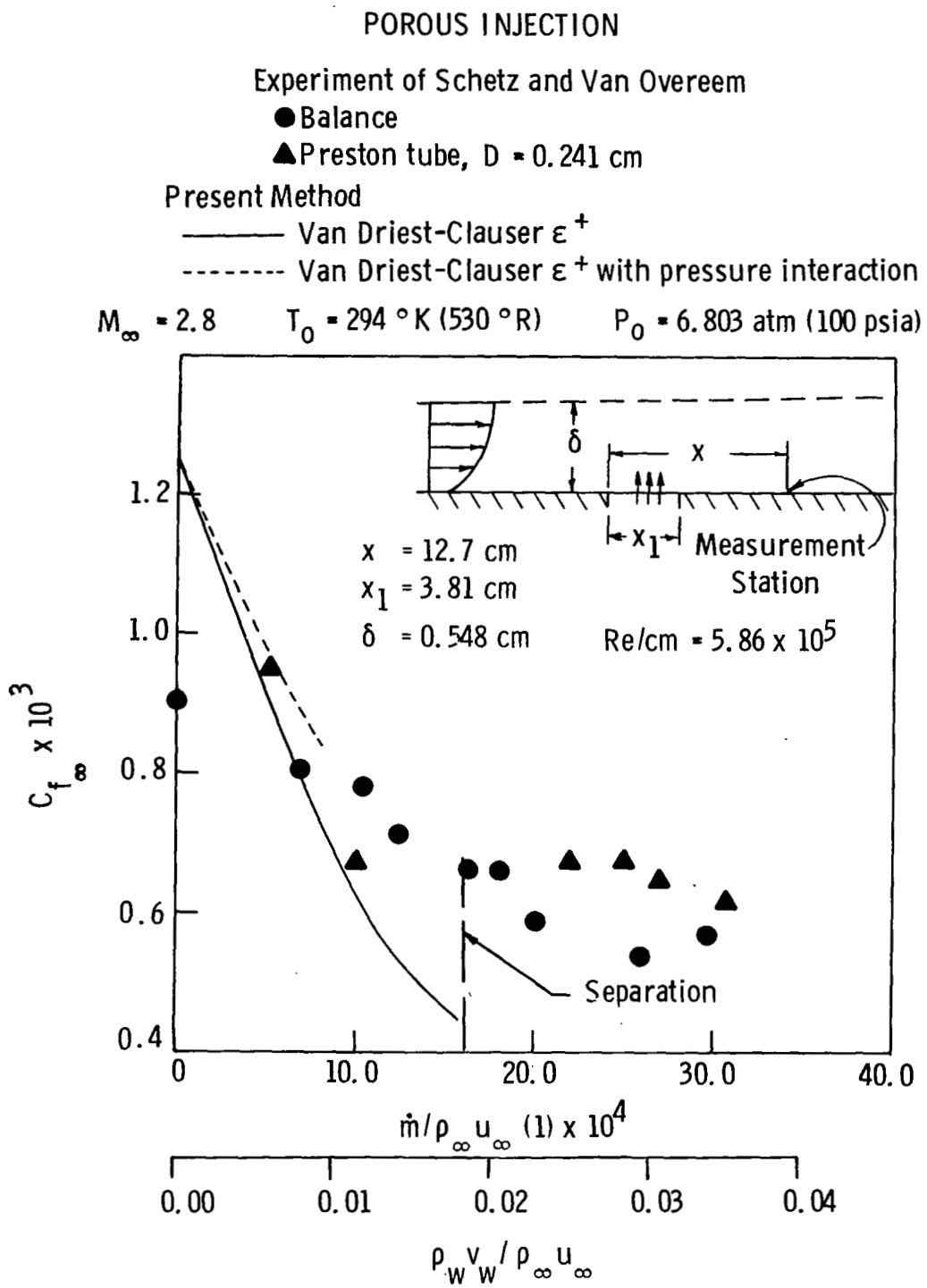

Figure 9: Skin Friction Coefficient Variation with Mass Flow Rate, Porous Injection, Station 1

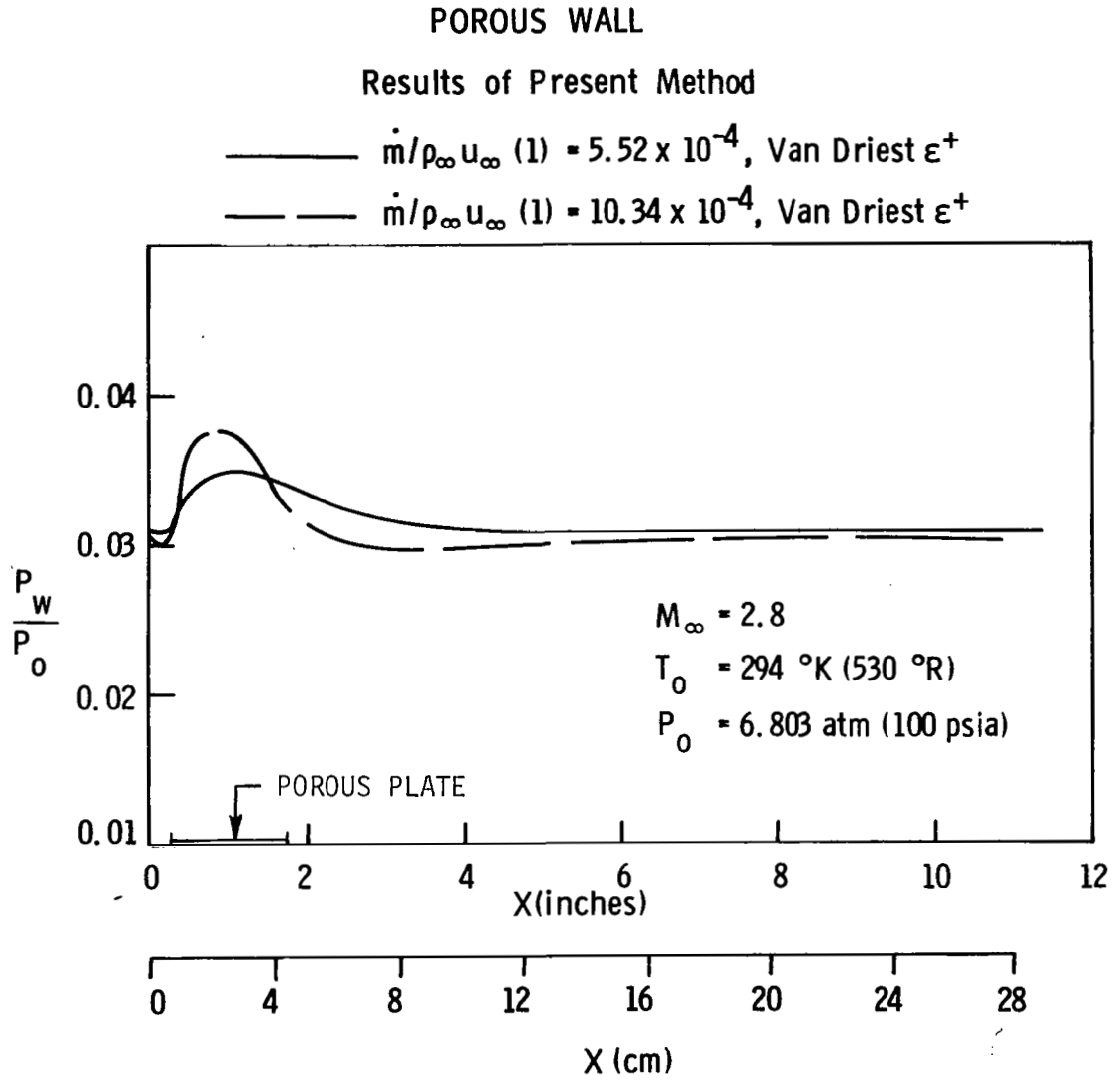

Figure 10: Predicted Wall Pressure Distribution for Porous Plate Injection

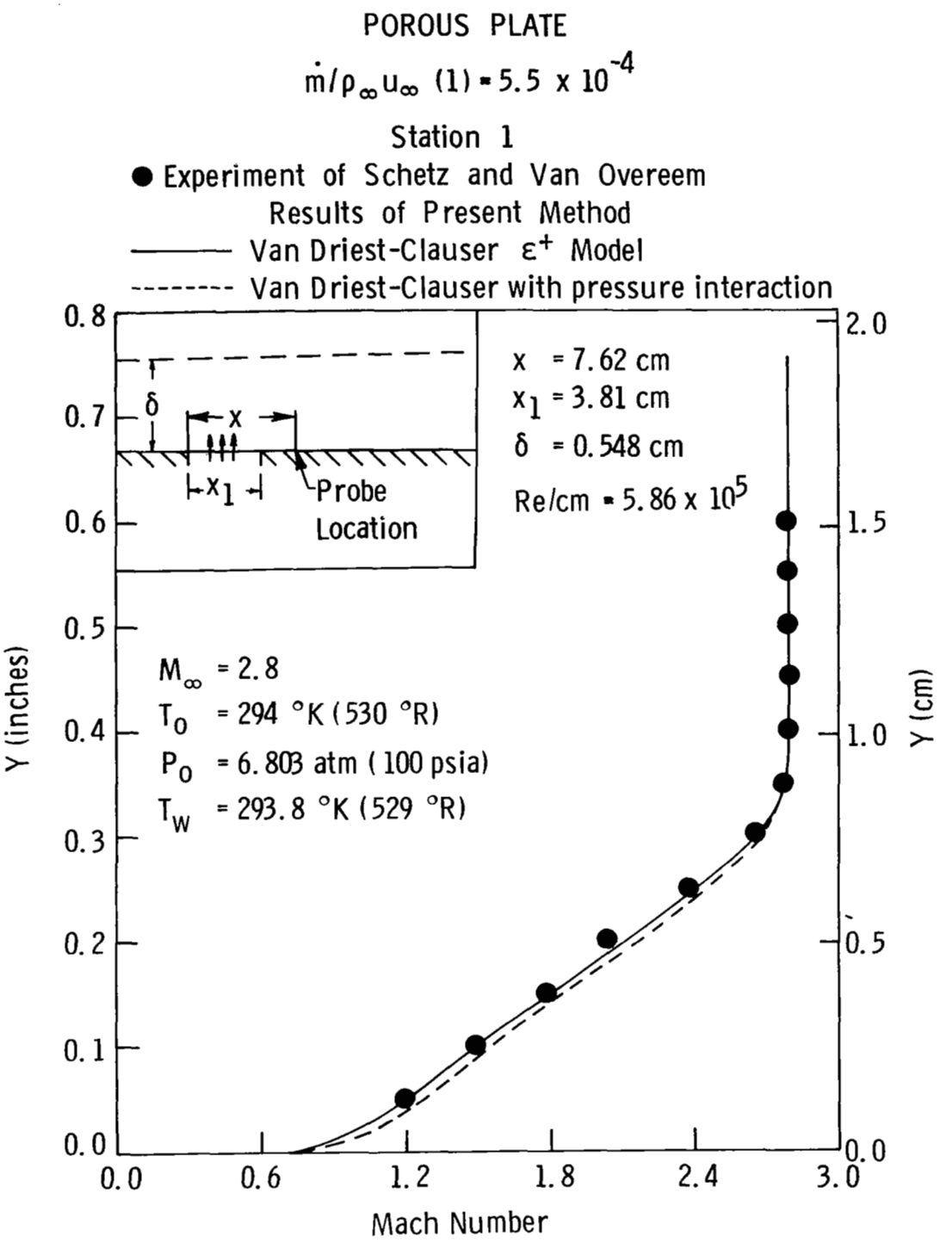

Figure 11: Porous Injection Mach Profiles, Low Mass Injection, Station 1

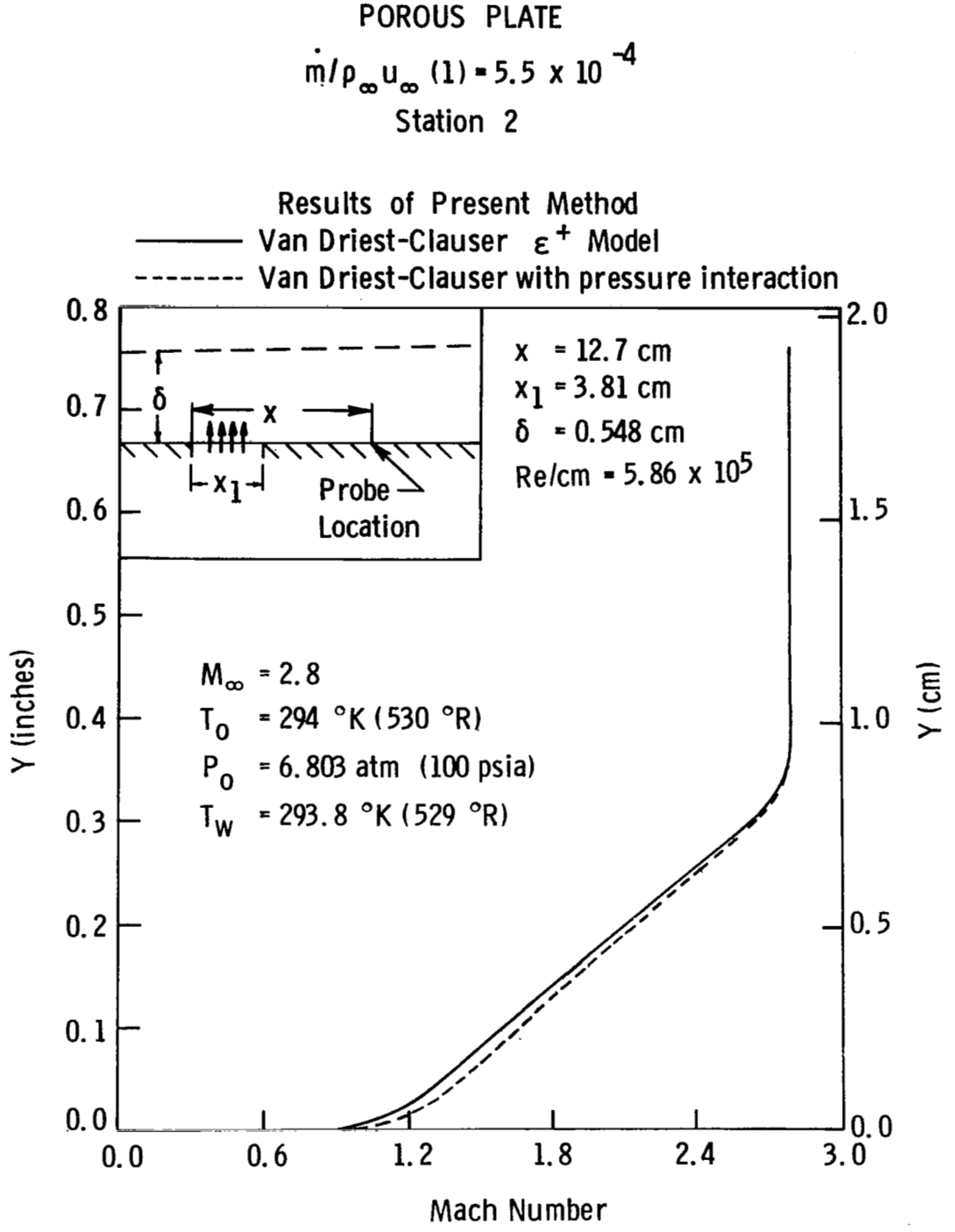

Figure 12: Porous Injection Mach Profiles, Low Mass Injection, Station 2

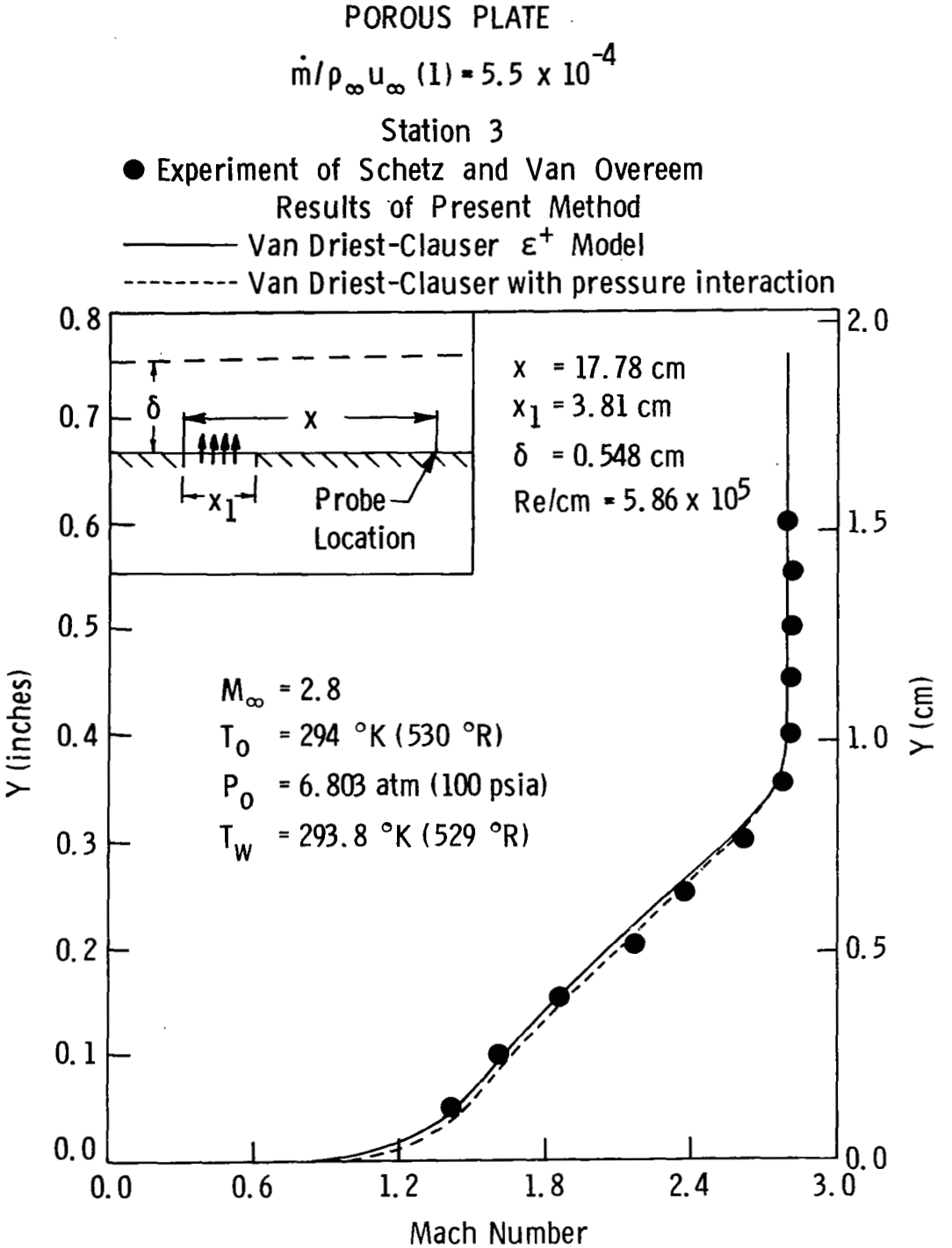

Figure 13: Porous Injection Mach Profiles, Low Mass Injection, Station 3

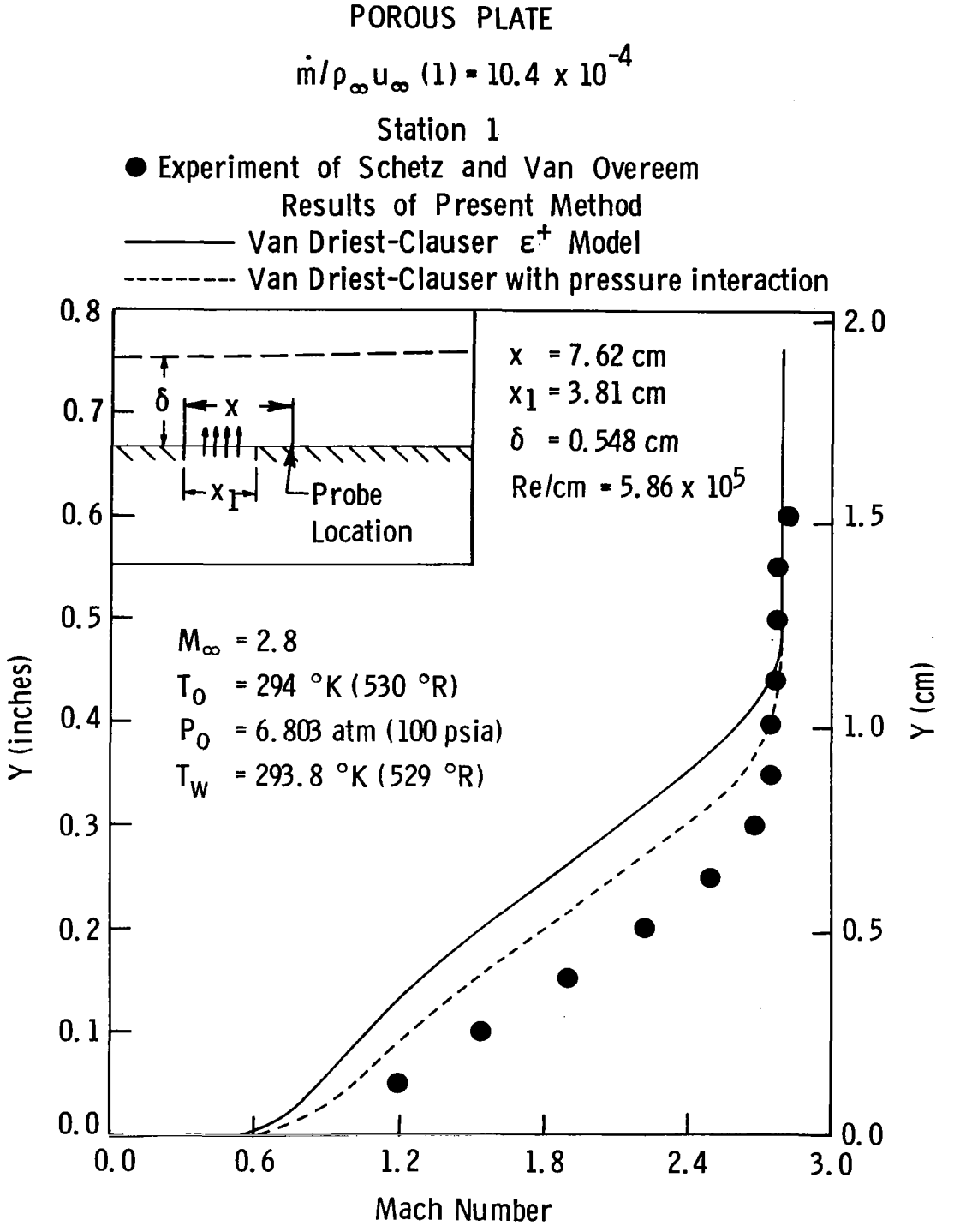

Figure 14: Porous Injection Mach Profiles, High Mass Injection, Station 1

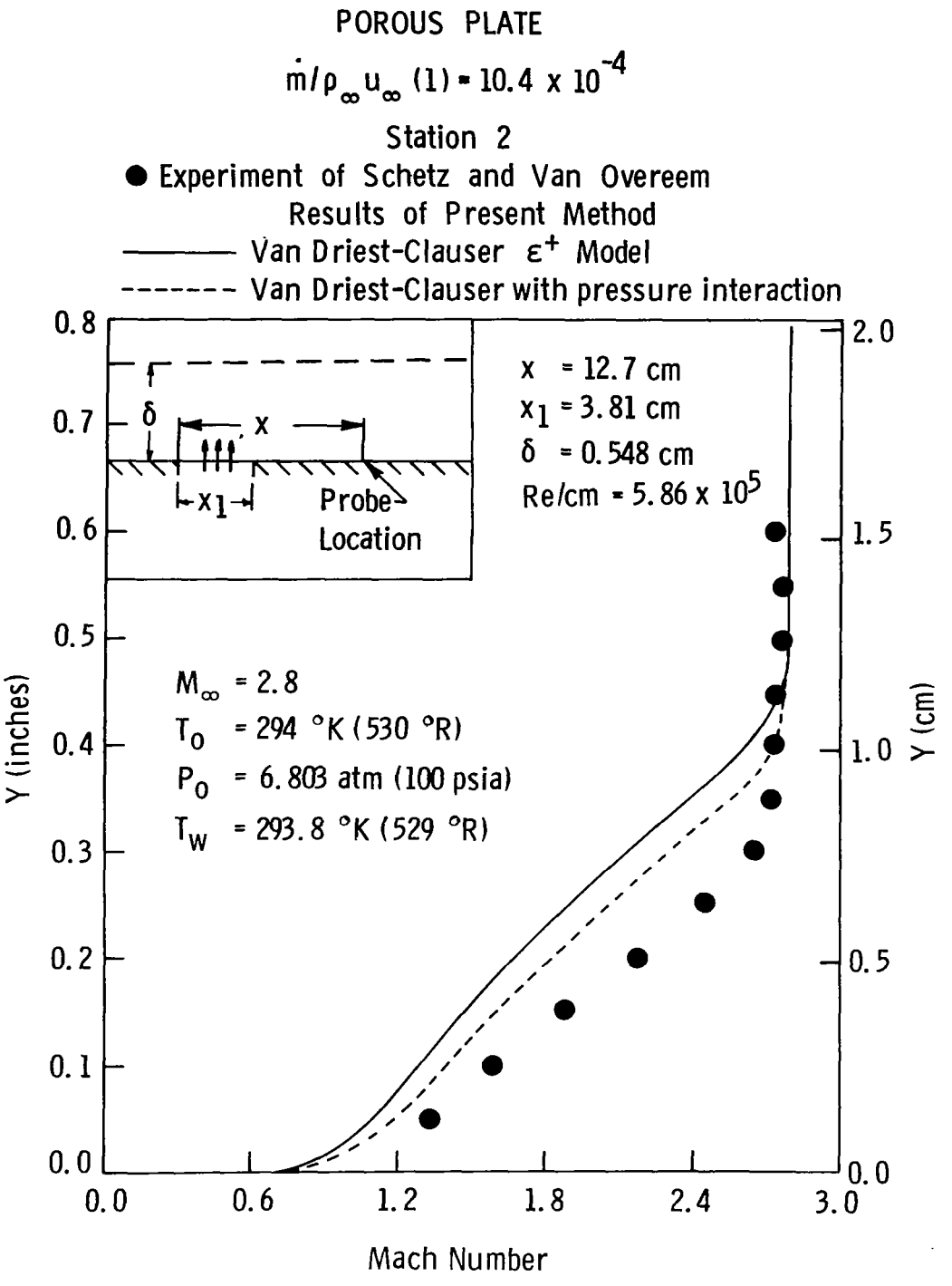

Figure 15: Porous Injection Mach Profiles, High Mass Injection, Station 2

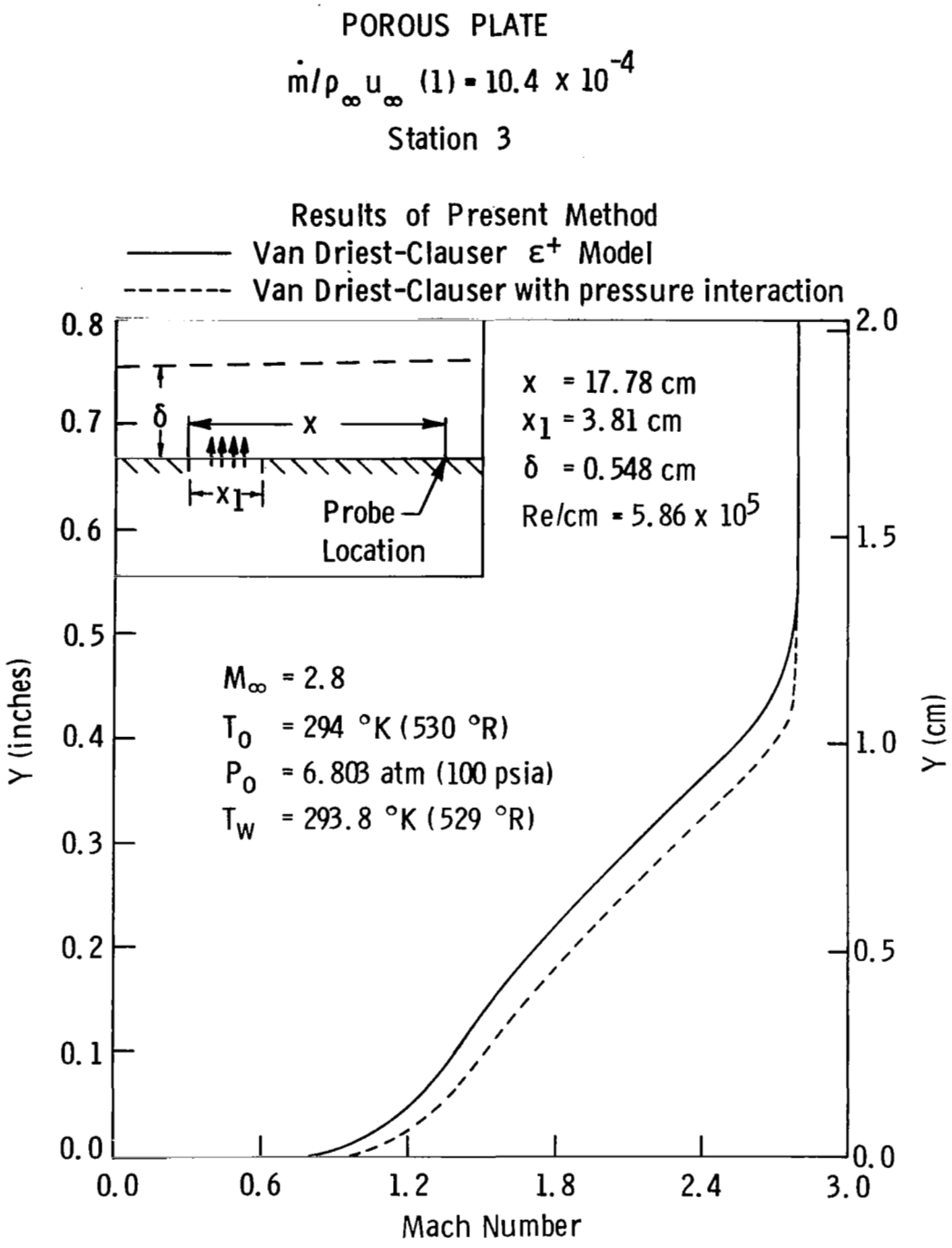

Figure 16: Porous Injection Mach Profiles, High Mass Injection, Station 3

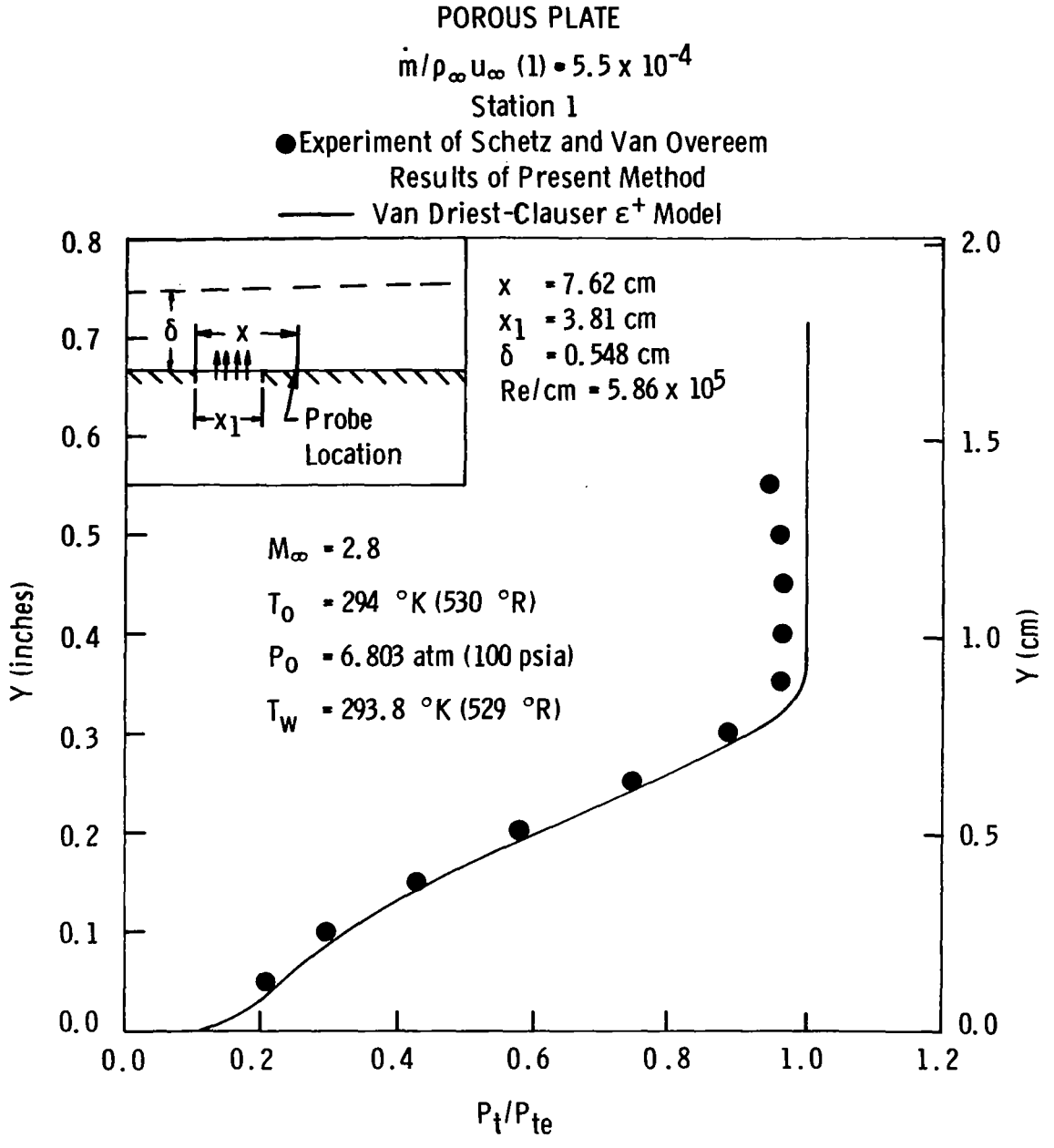

Figure 17: Porous Injection Pitot Pressure Profiles, Low Mass Injection, Station 1

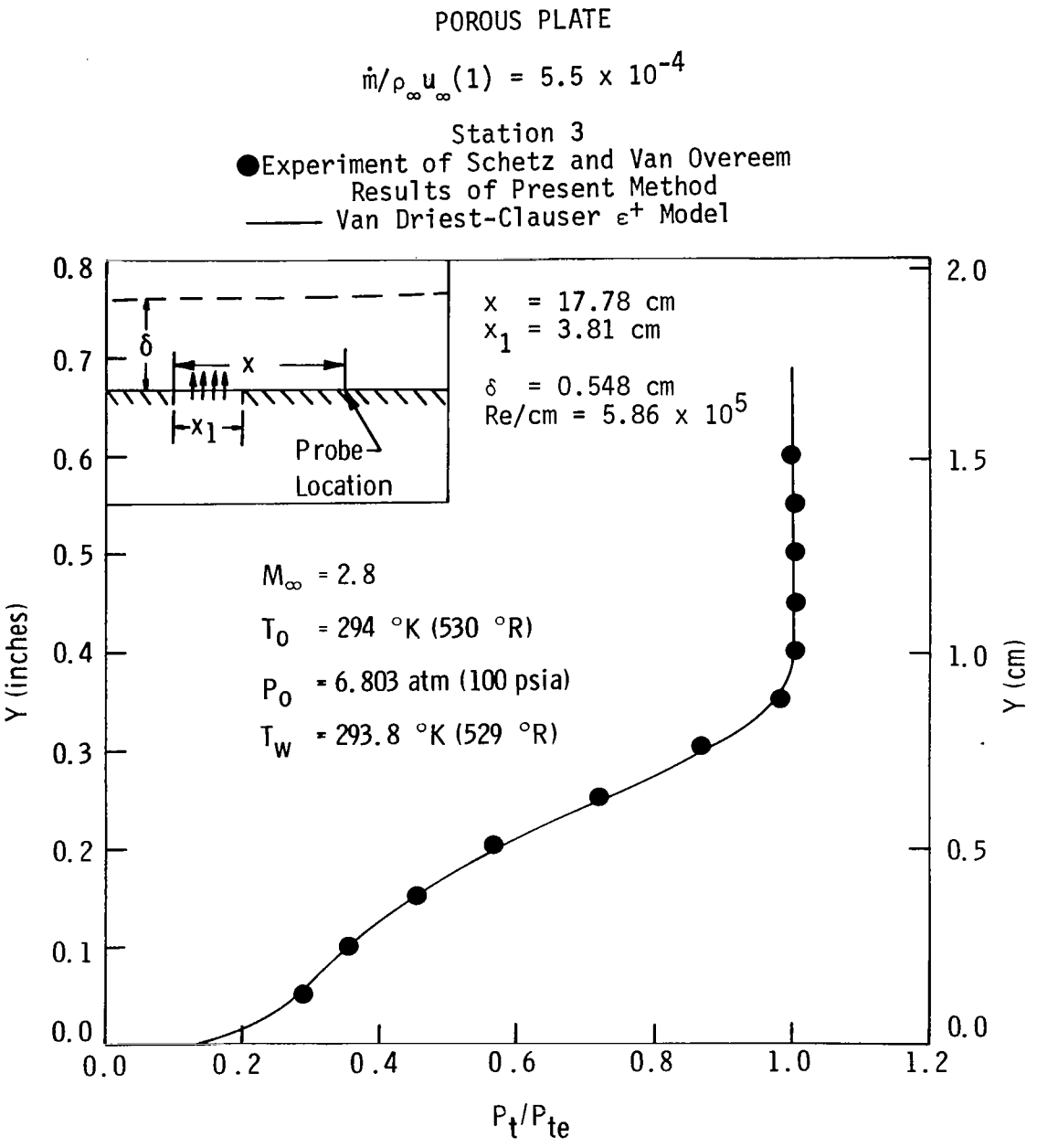

Figure 18: Porous Injection Pitot Profiles, Low Mass Injection, Station 3

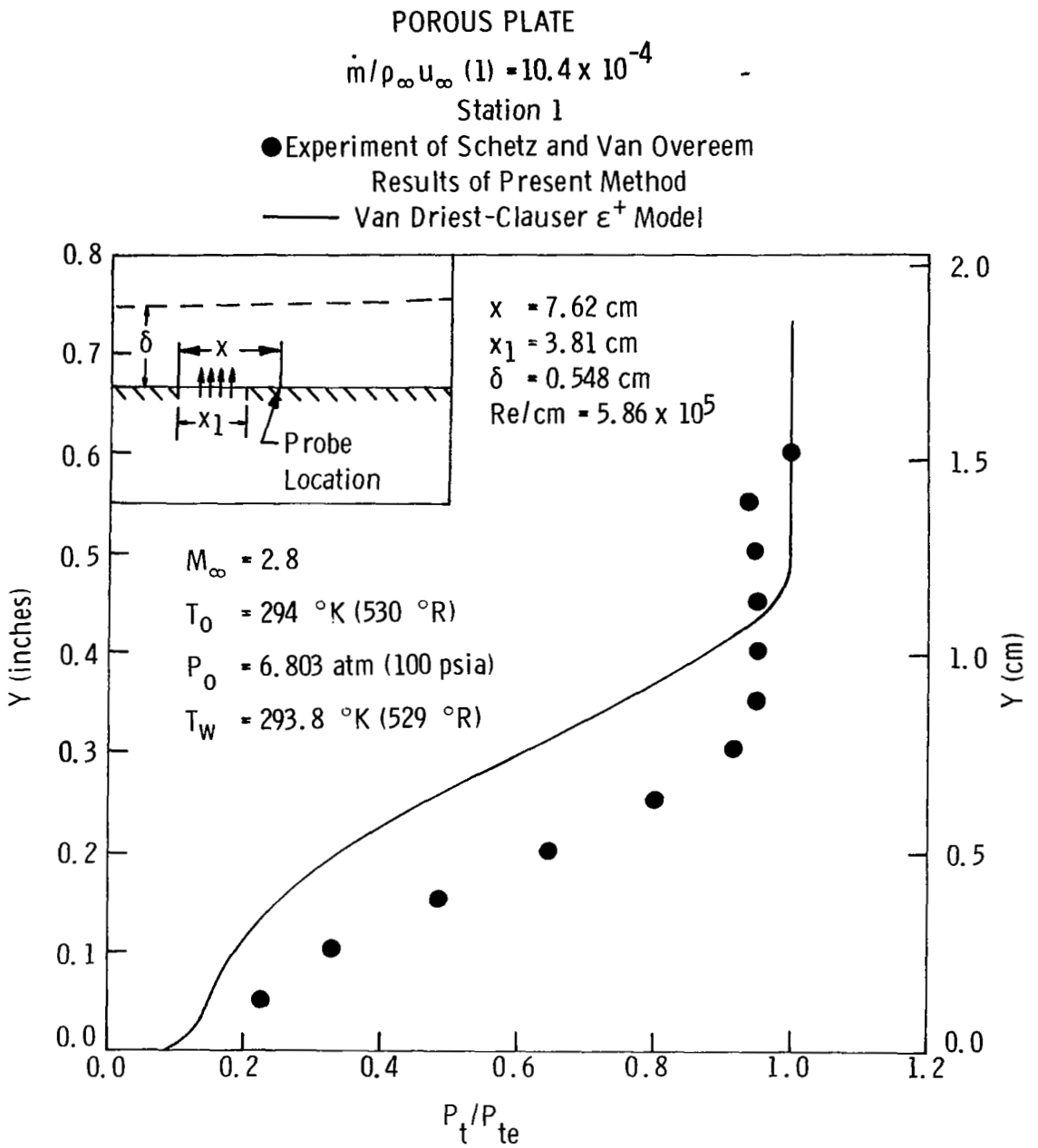

Figure 19: Porous Injection Pitot Pressure Profiles, High Mass Injection, Station 1

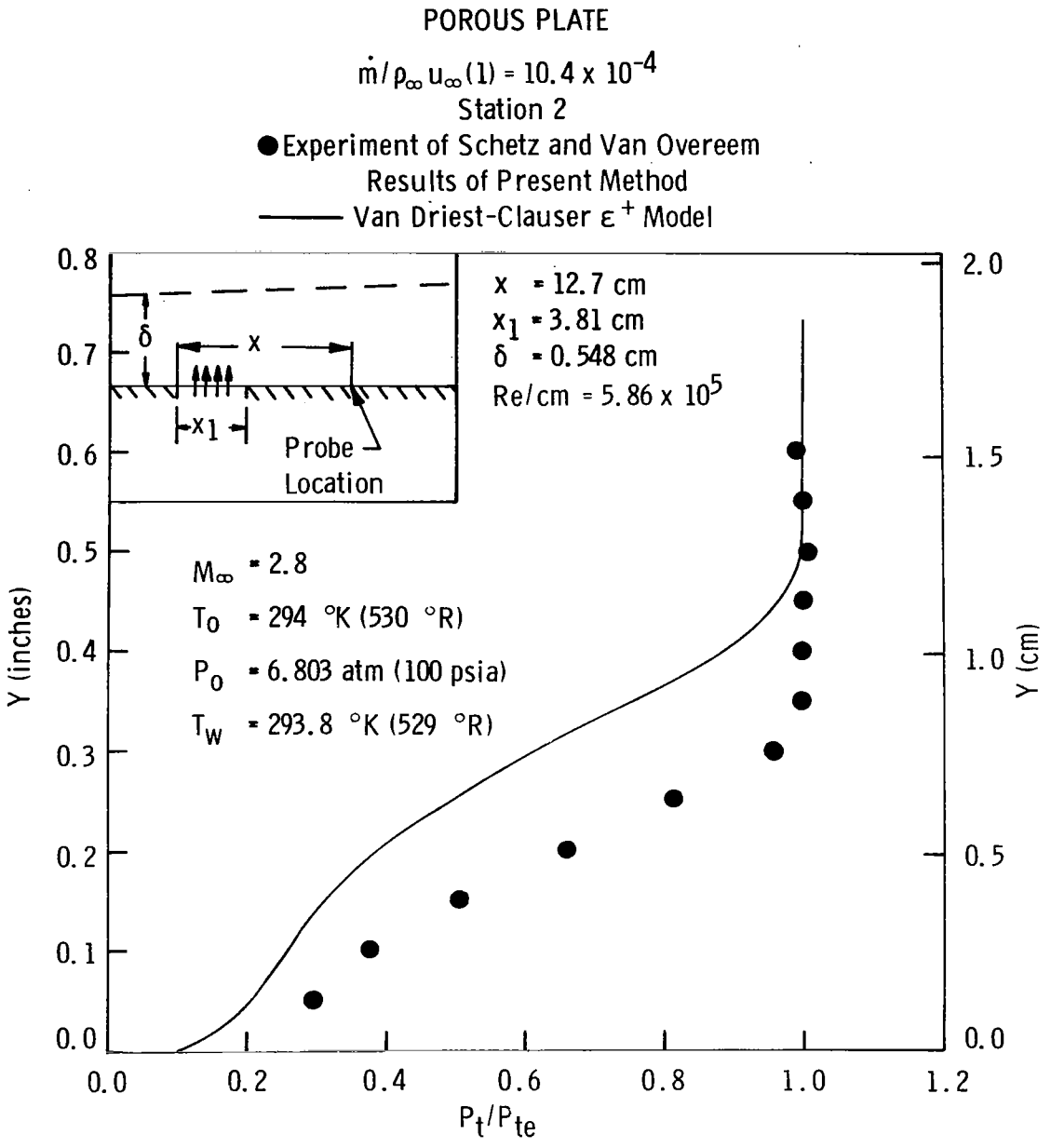

Figure 20: Porous Injection Pitot Pressure Profiles, High Mass Injection, Station 2

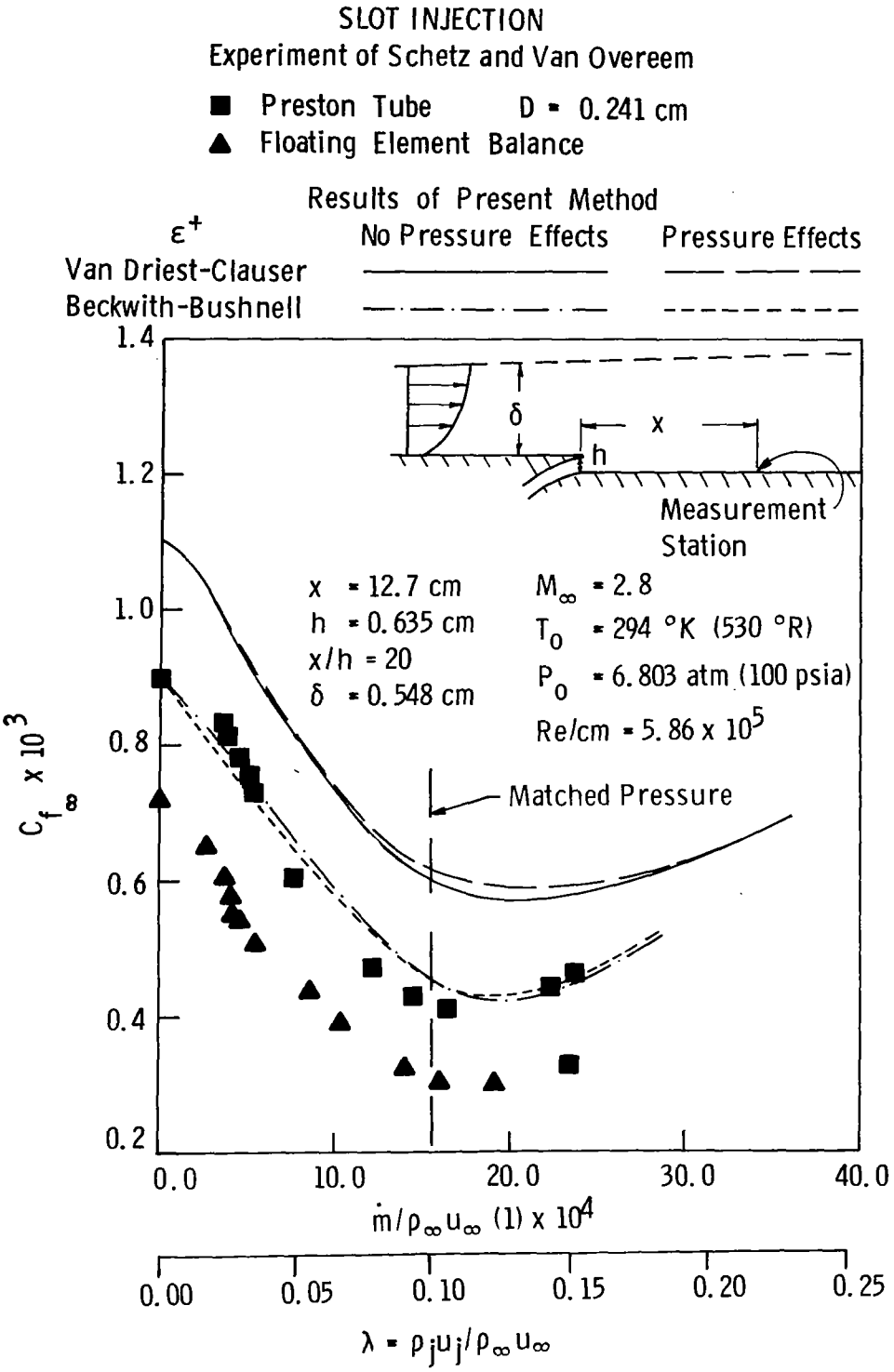

Figure 21: Skin Friction Coefficient Variation with Mass Flow Rate, Slot Injection, Station 2

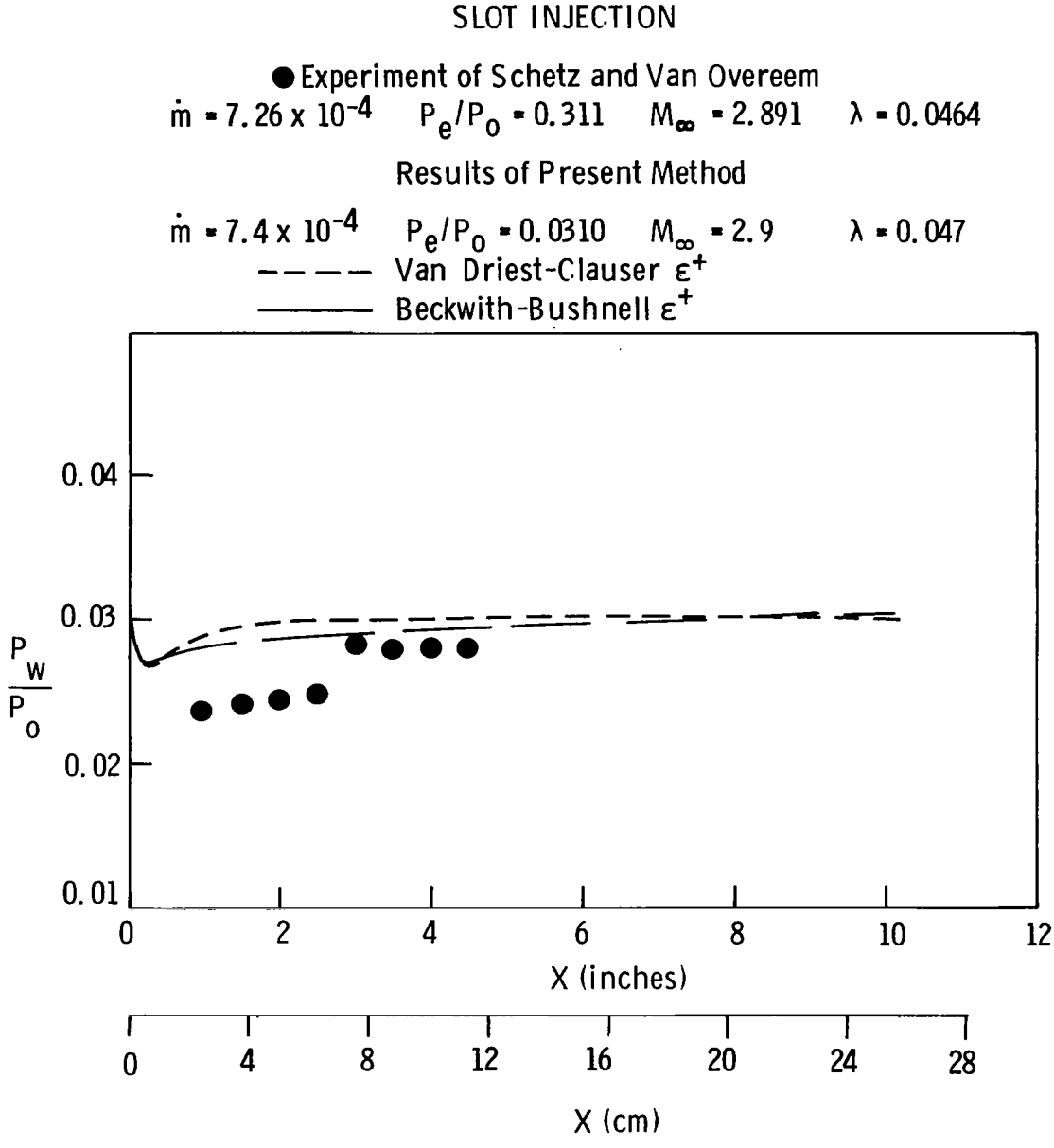

Figure 22: Wall Pressure Distribution, Slot Injection

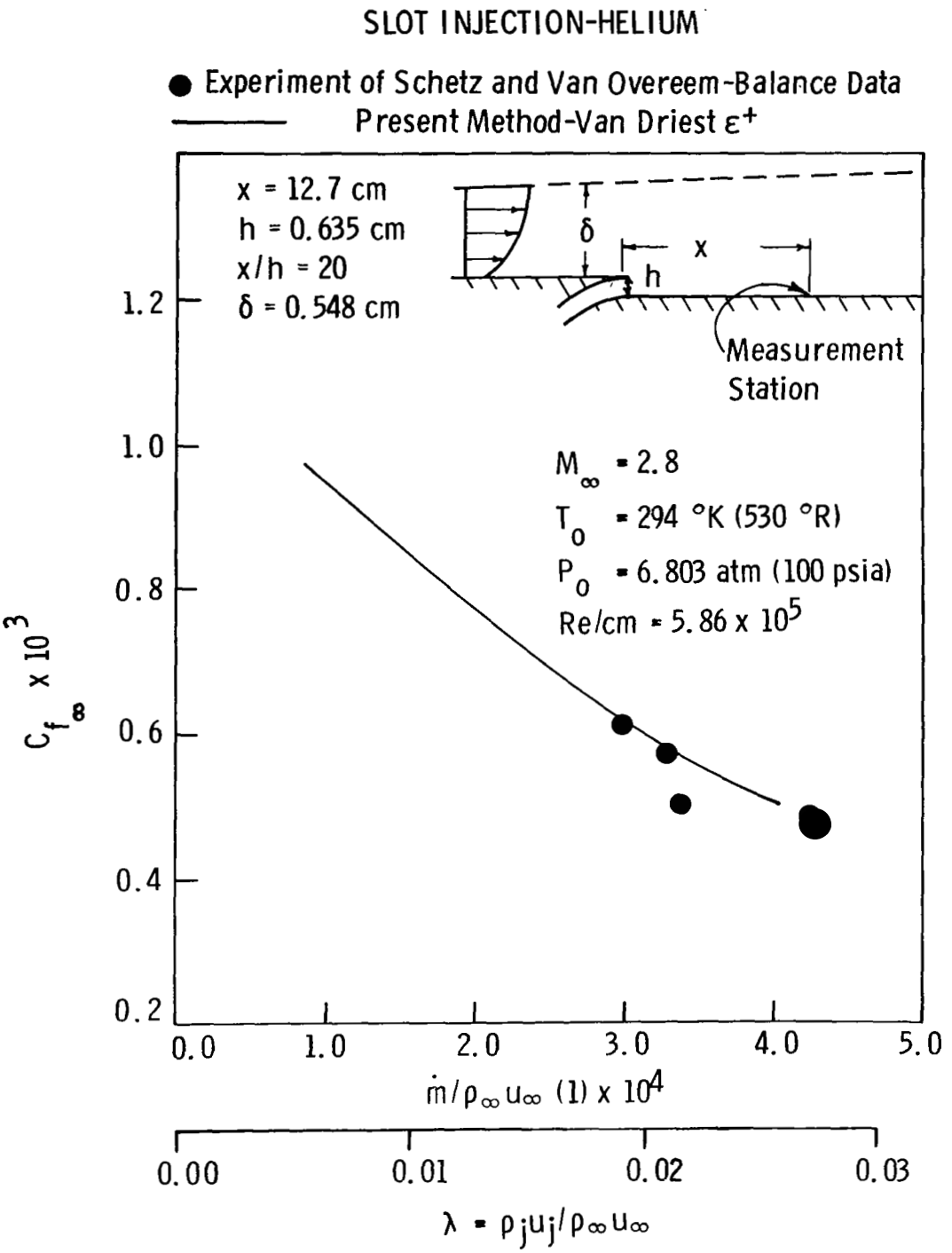

Figure 23: Skin Friction Coefficient Variation with Mass Flow Rate, Helium Slot Injection, Station 2

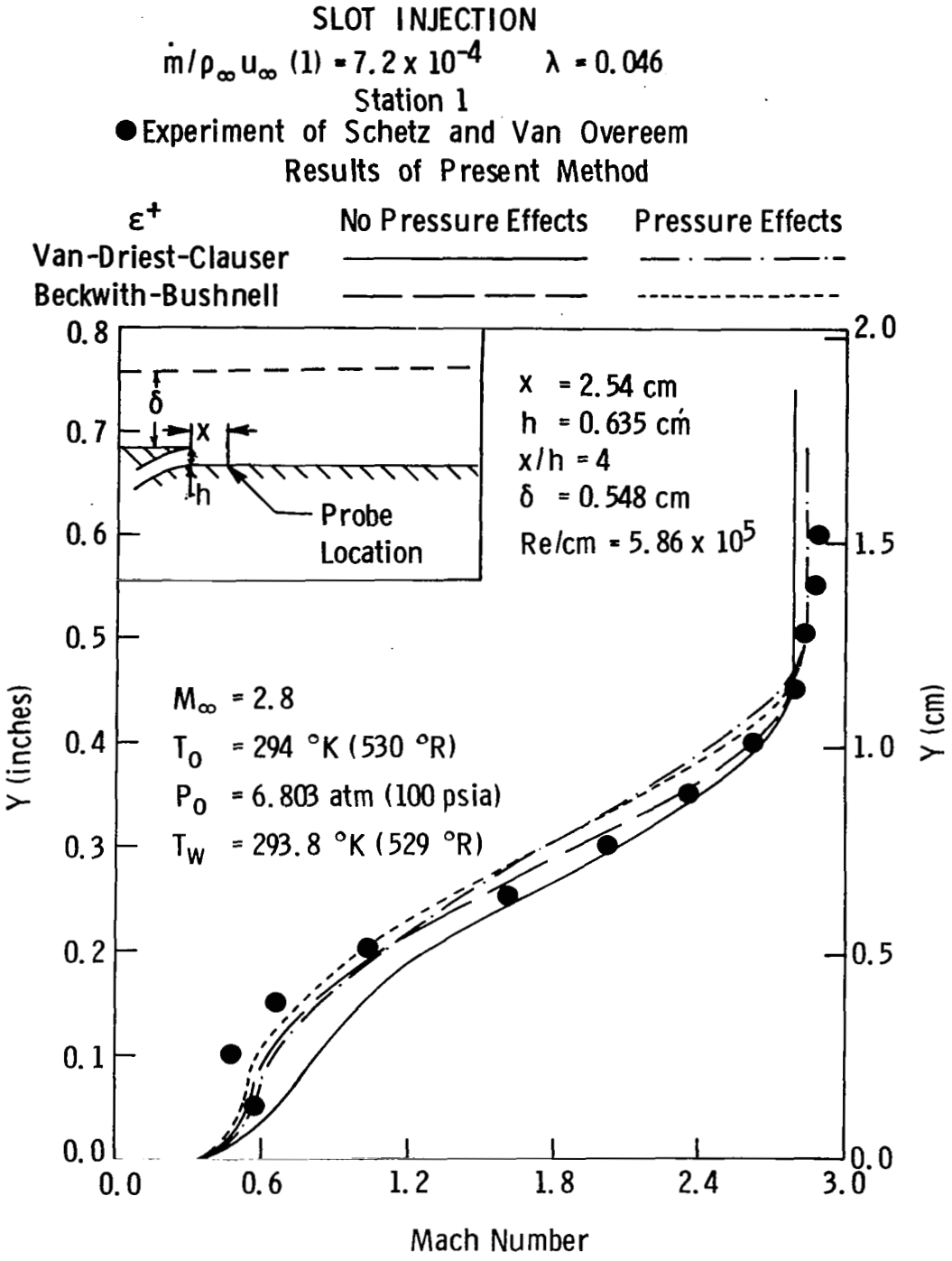

Figure 24: Slot Injection Mach Profiles, Low Mass Injection, Station 1

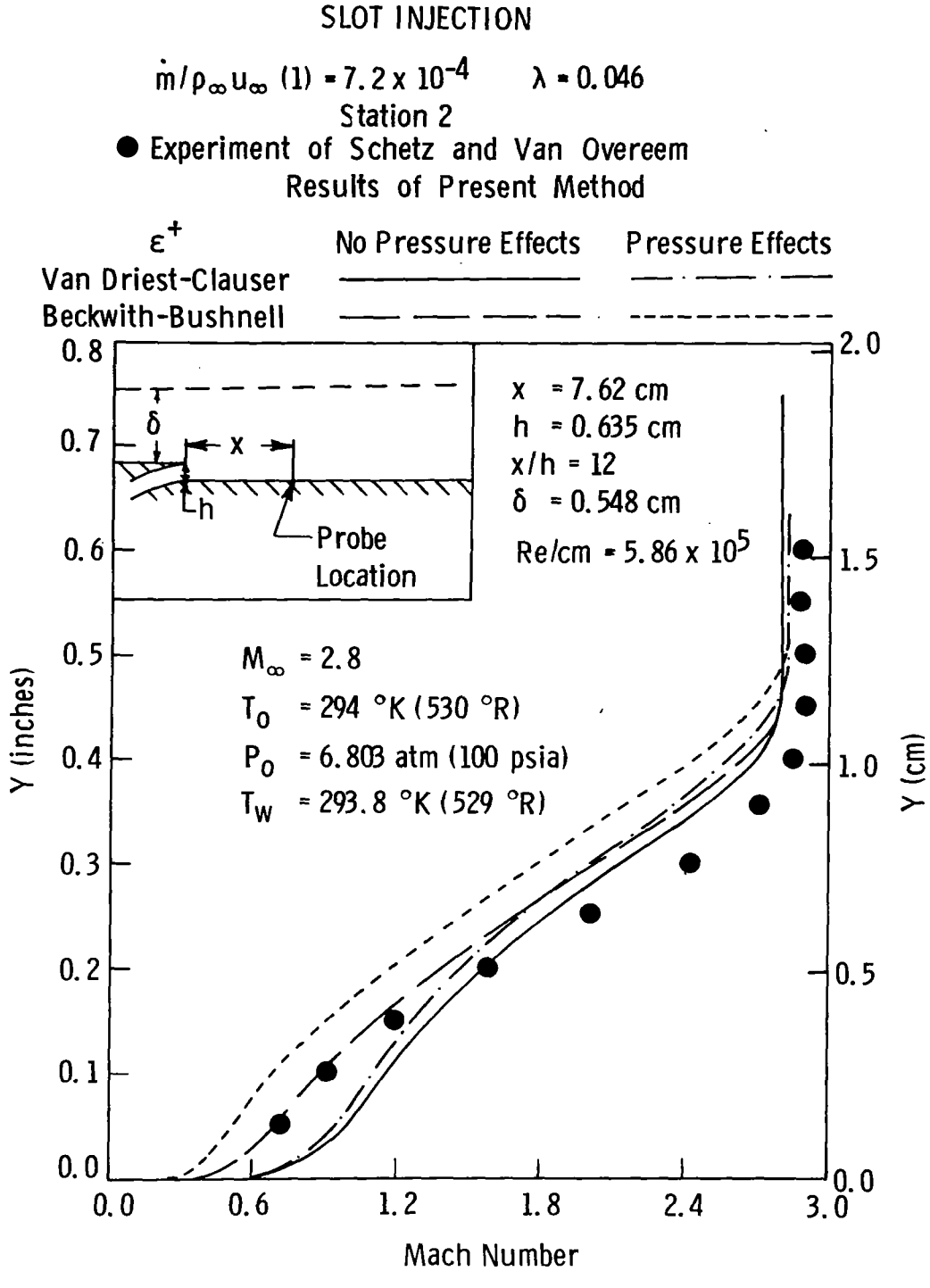

Figure 25: Slot Injection Mach Profiles, Low Mass Injection, Station 2

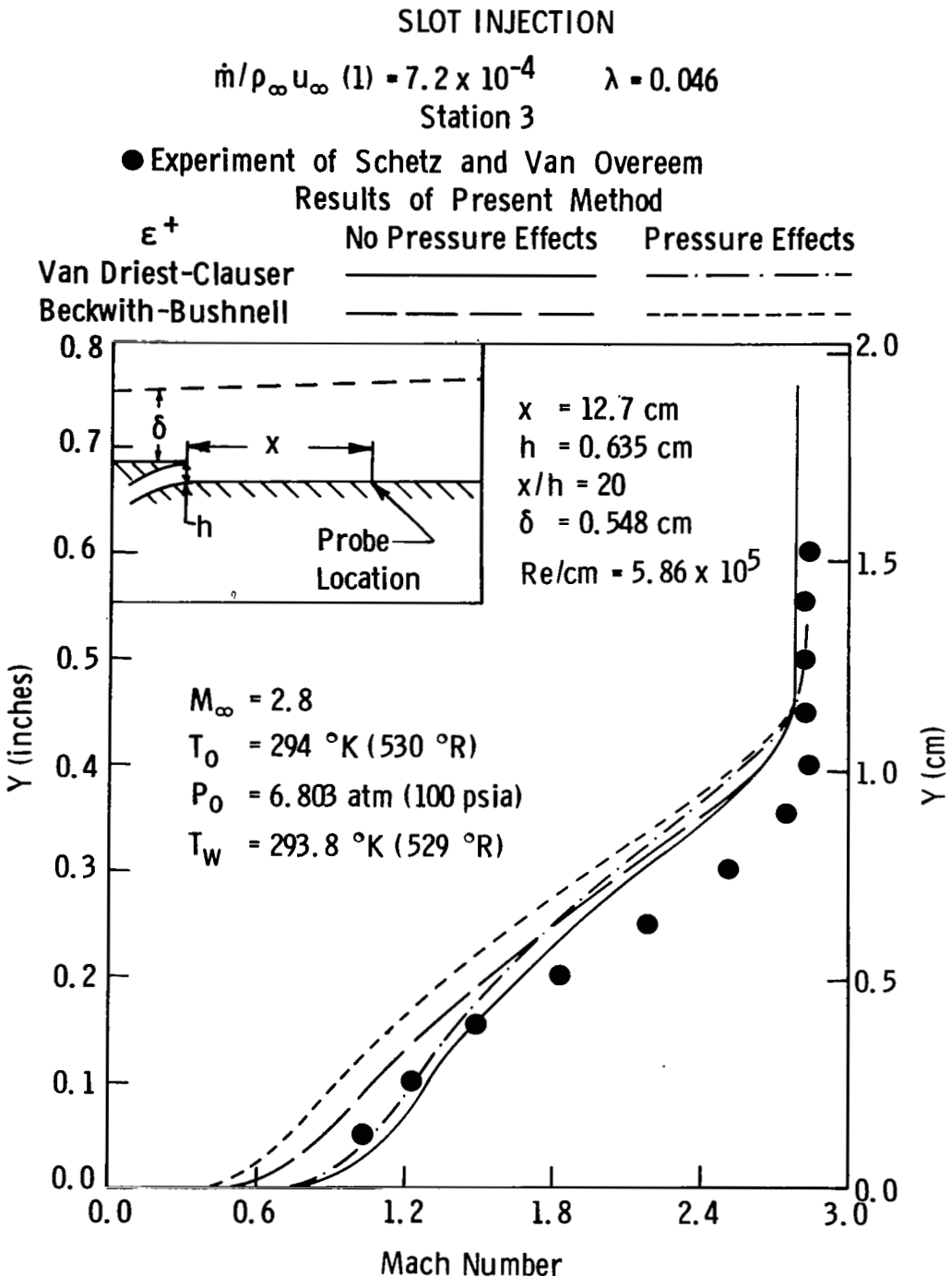

Figure 26: Slot Injection Mach Profiles, Low Mass Injection, Station 3

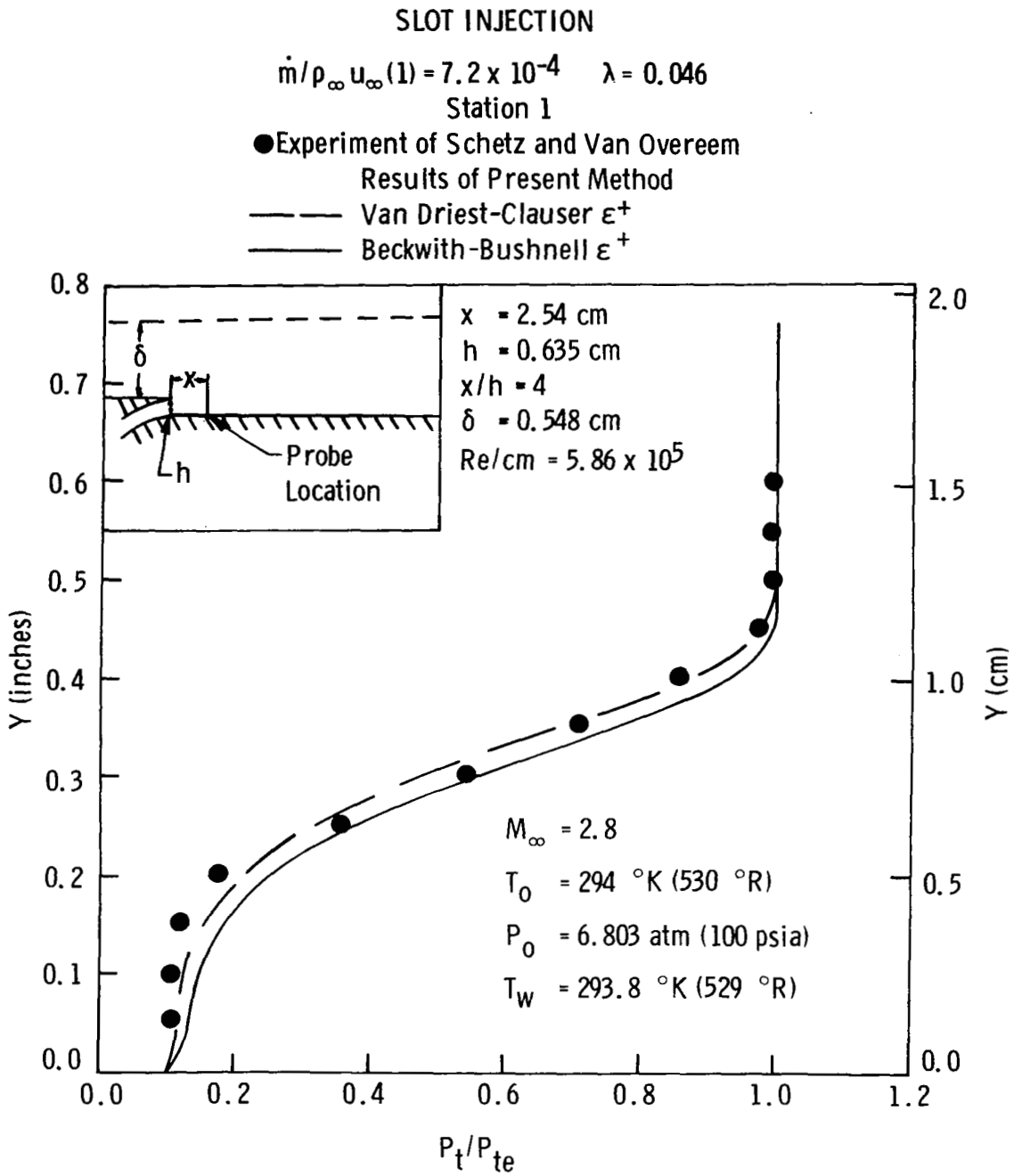

Figure 27: Slot Injection Pitot Pressure Profiles, Low Mass Injection, Station 1

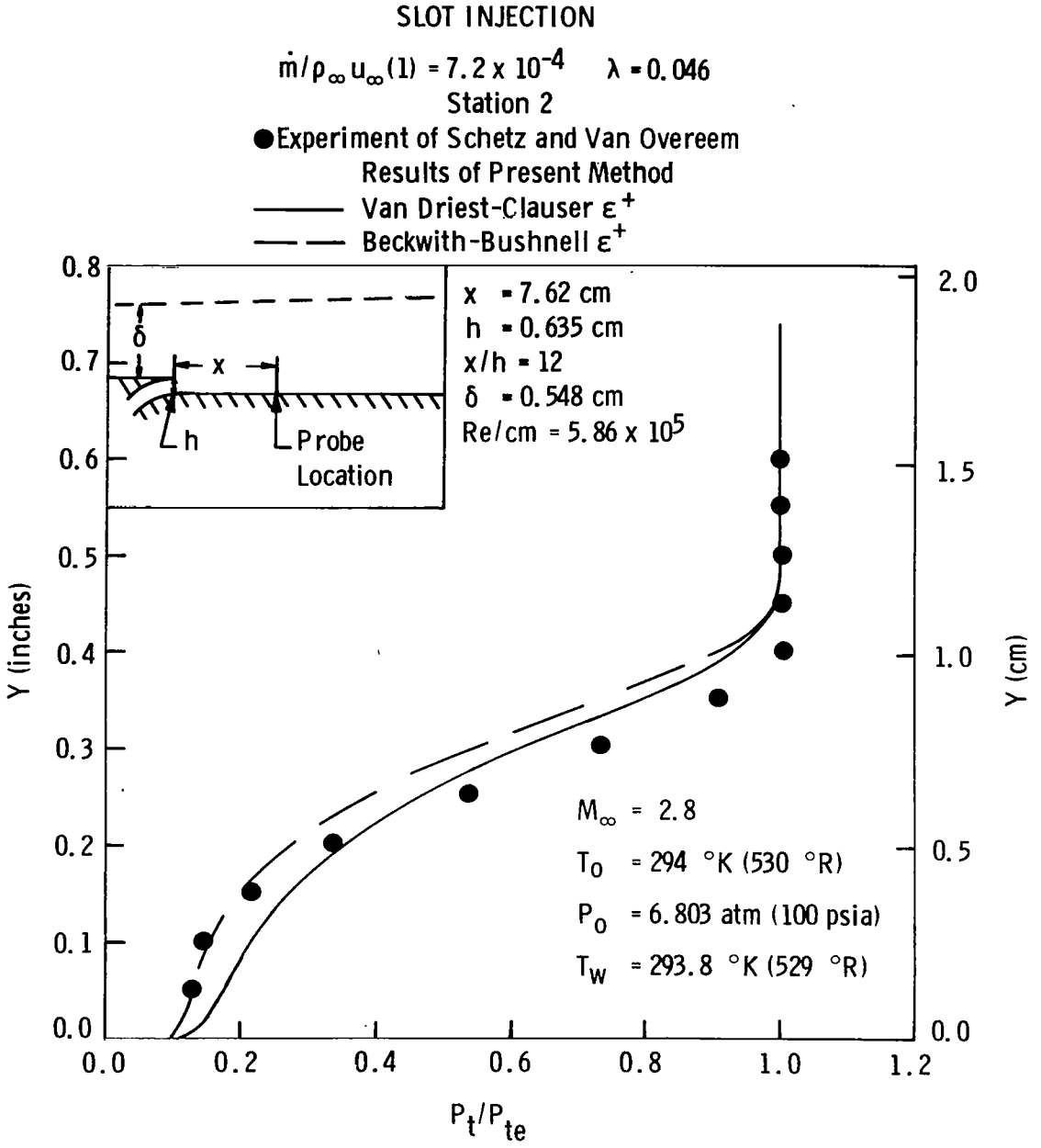

Figure 28: Slot Injection Pitot Pressure Profiles, Low Mass Injection, Station 2

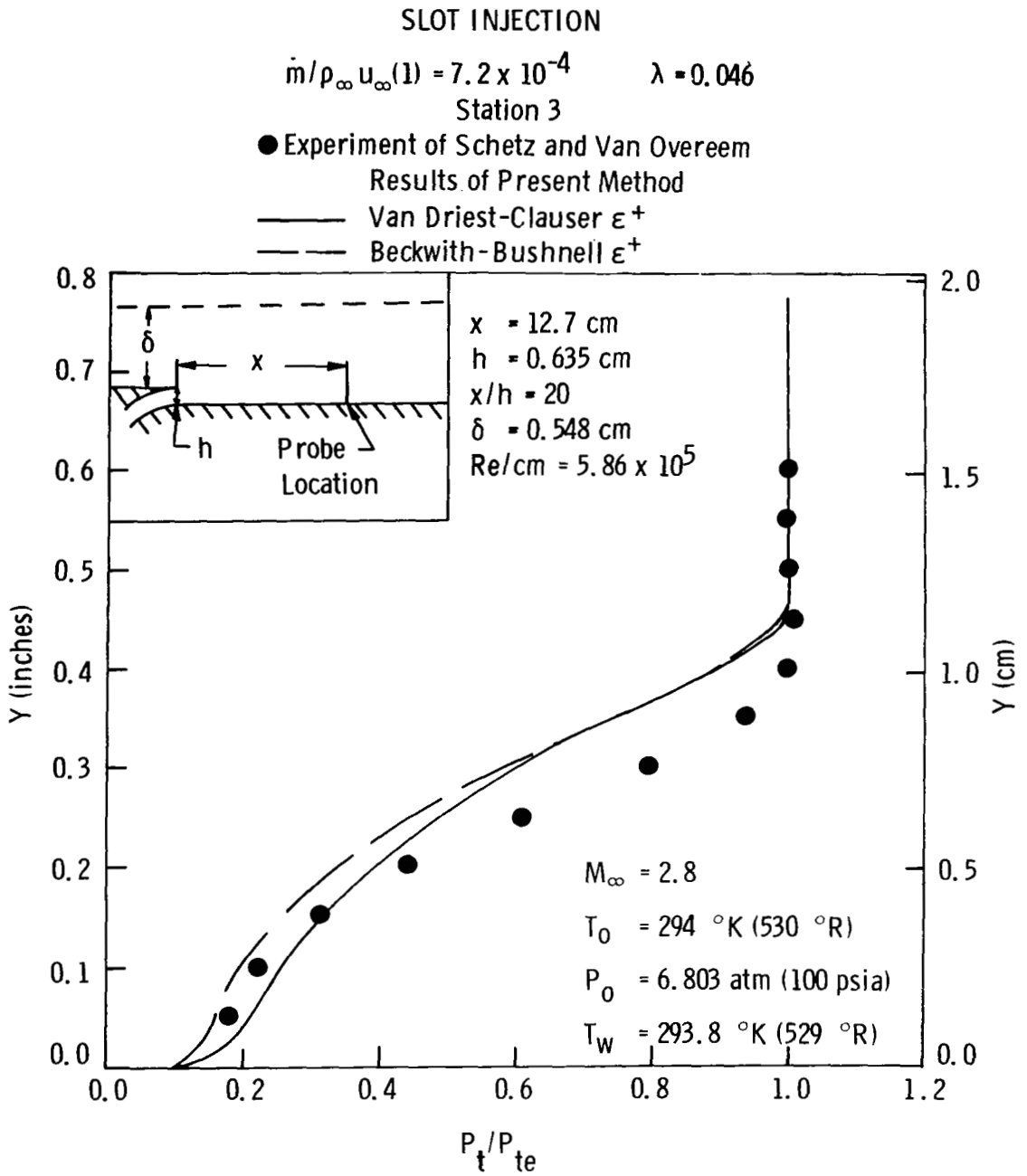

Figure 29: Slot Injection Pitot Pressure Profiles, Low Mass Injection, Station 3

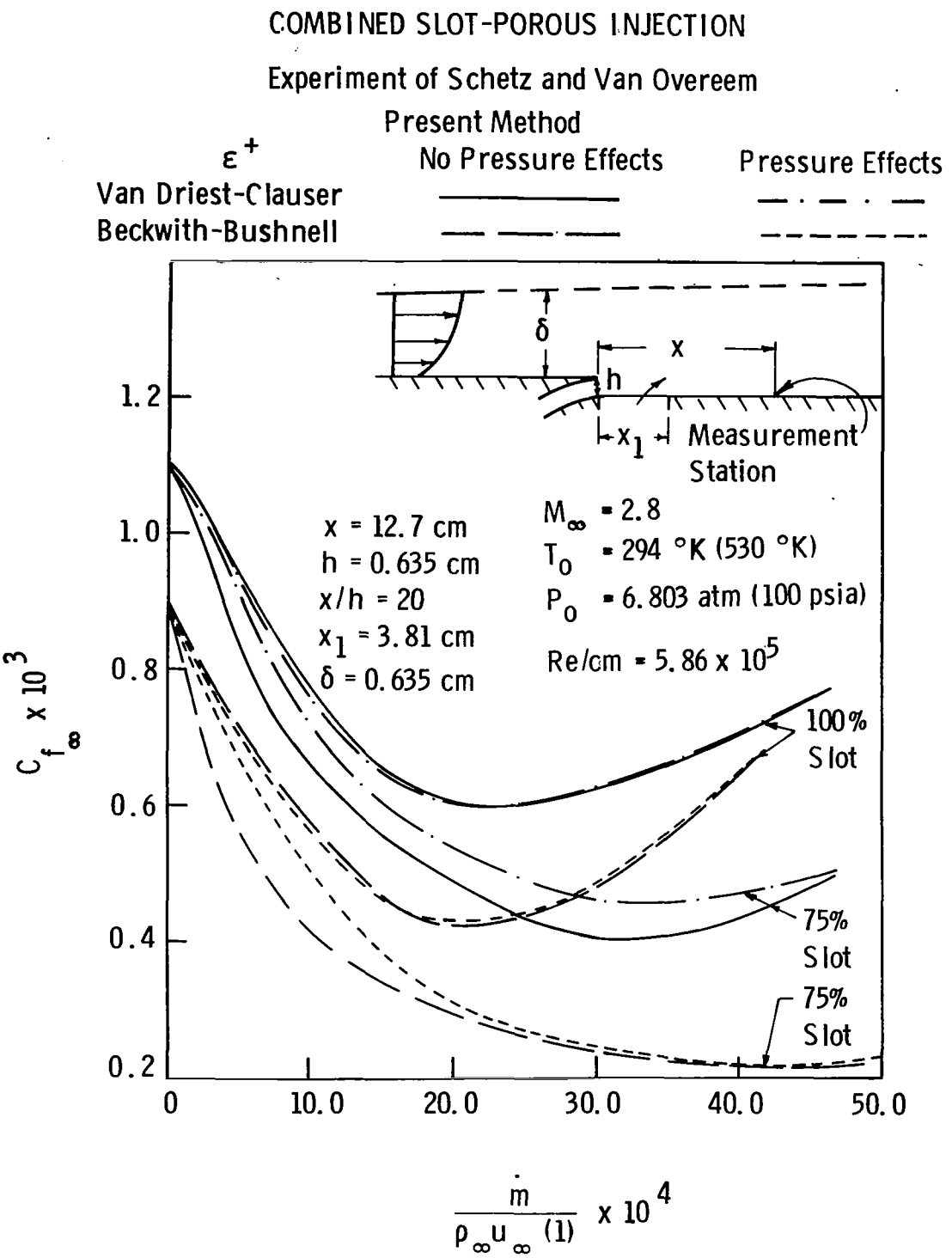

Figure 30: Skin Friction Coefficient Variation with Mass Flow Rate, Combined Injection, Station 2

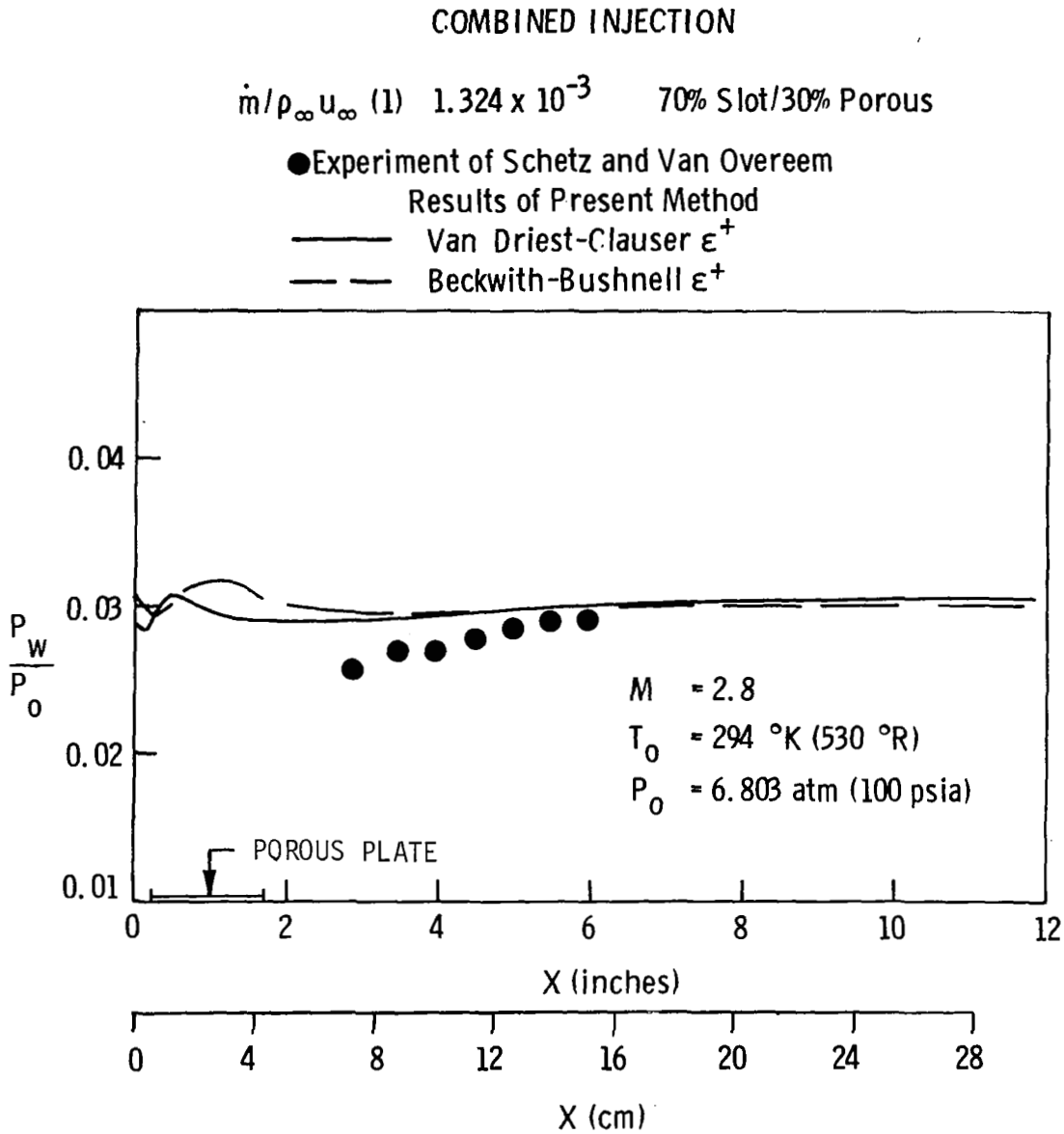

Figure 31: Wall Pressure Distribution, Combined Injection

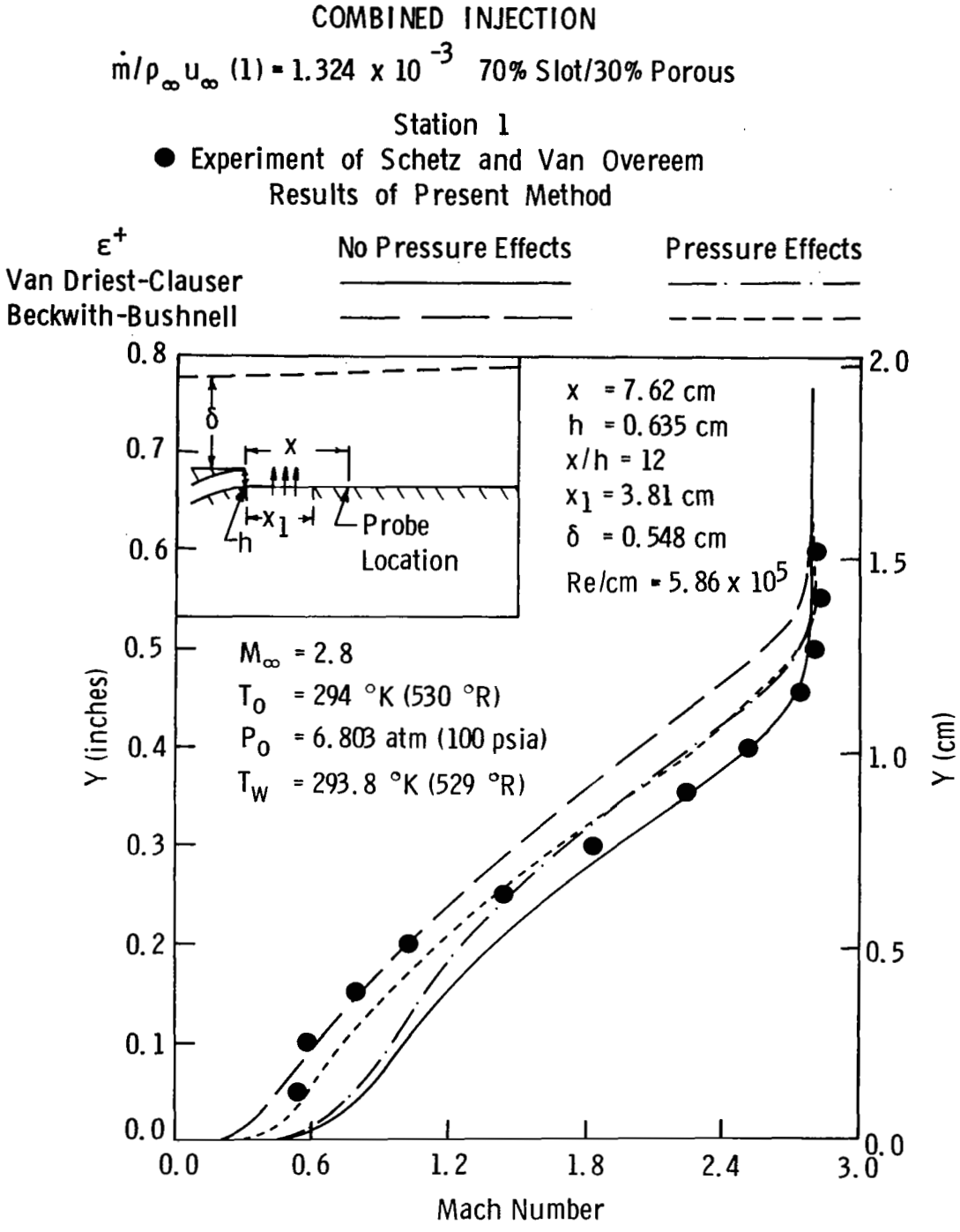

Figure 32: Combined Injection Mach Profiles, Station 1

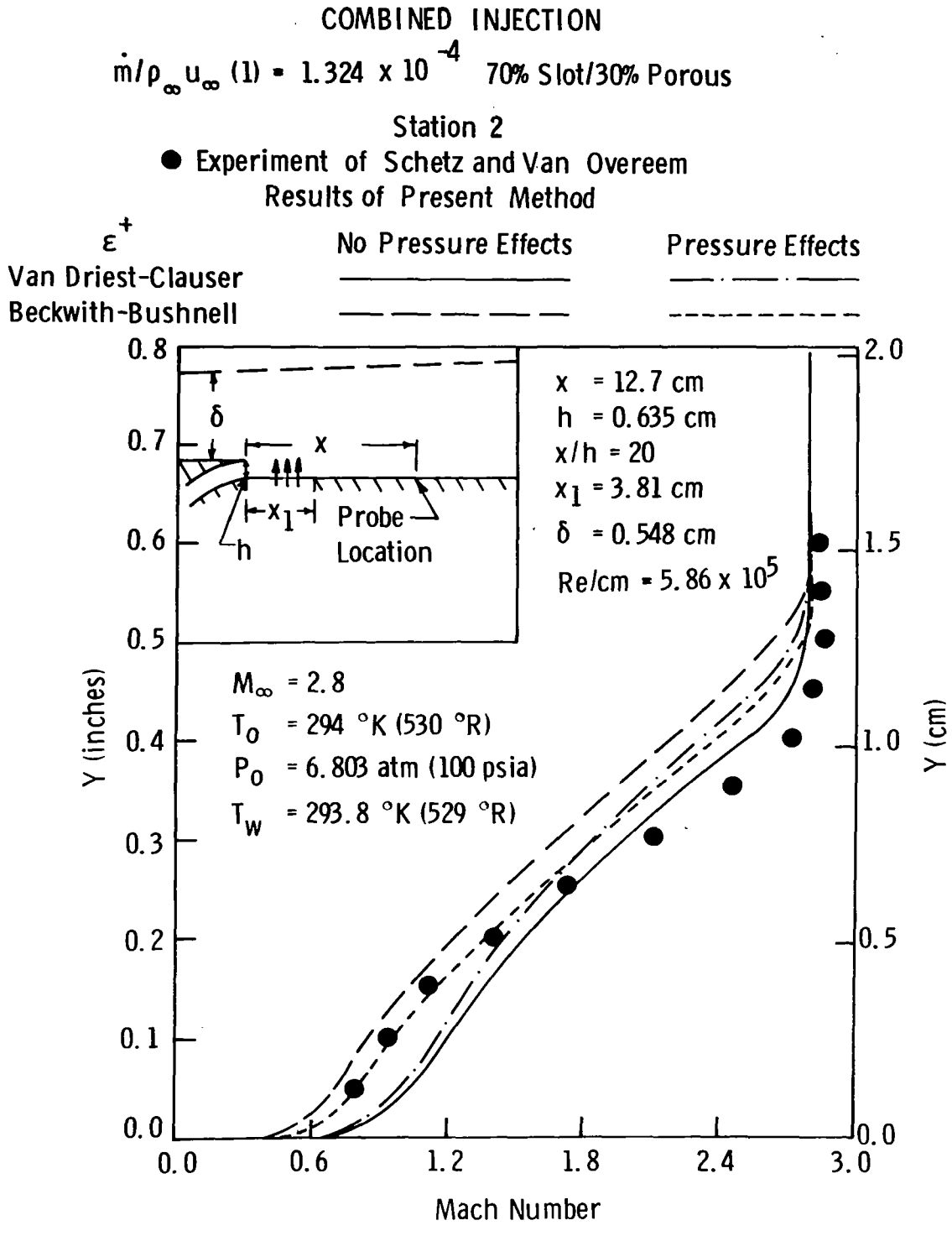

Figure 33: Combined Injection Mach Profiles, Station 2

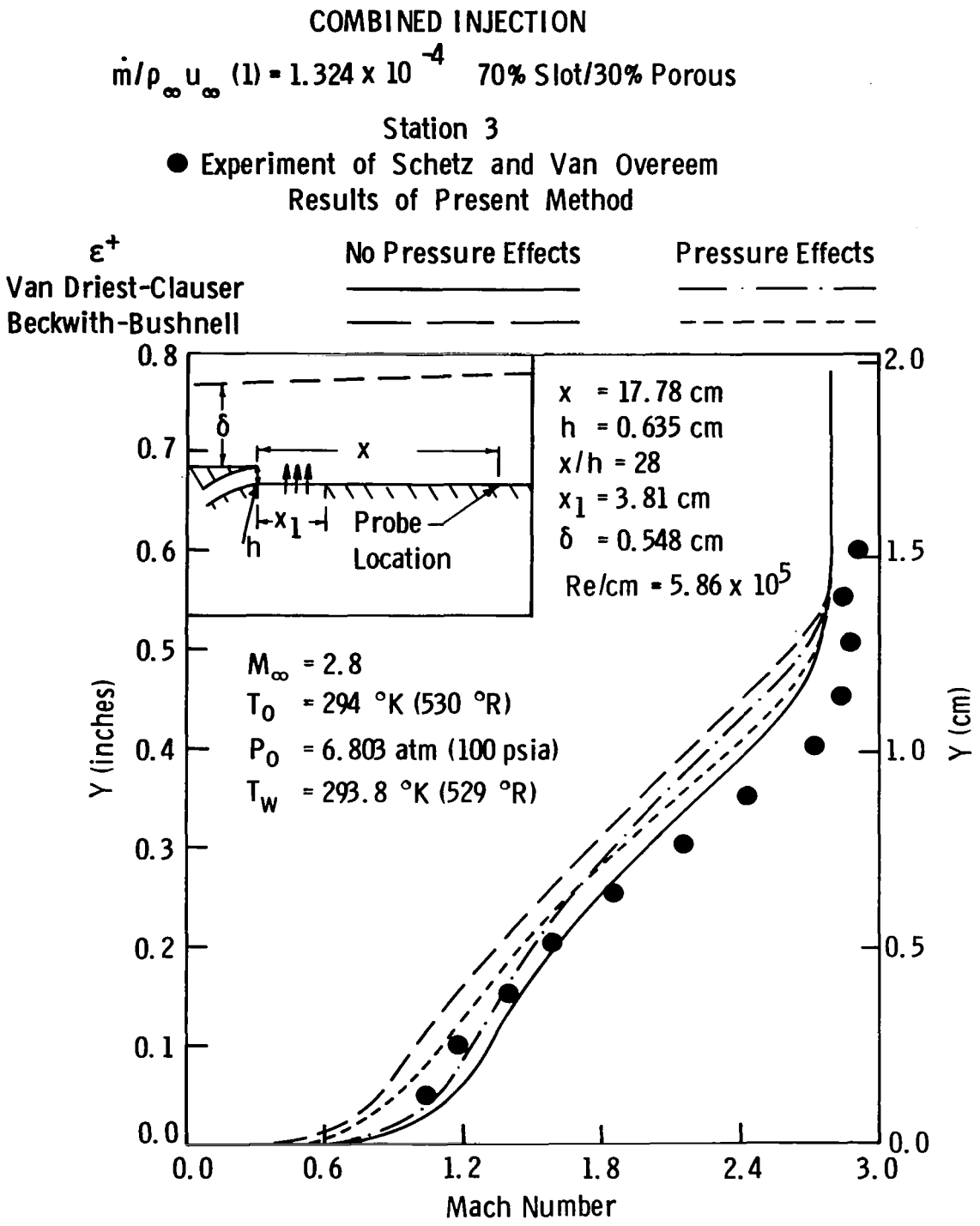

Figure 34: Combined Injection Mach Profiles, Station 3

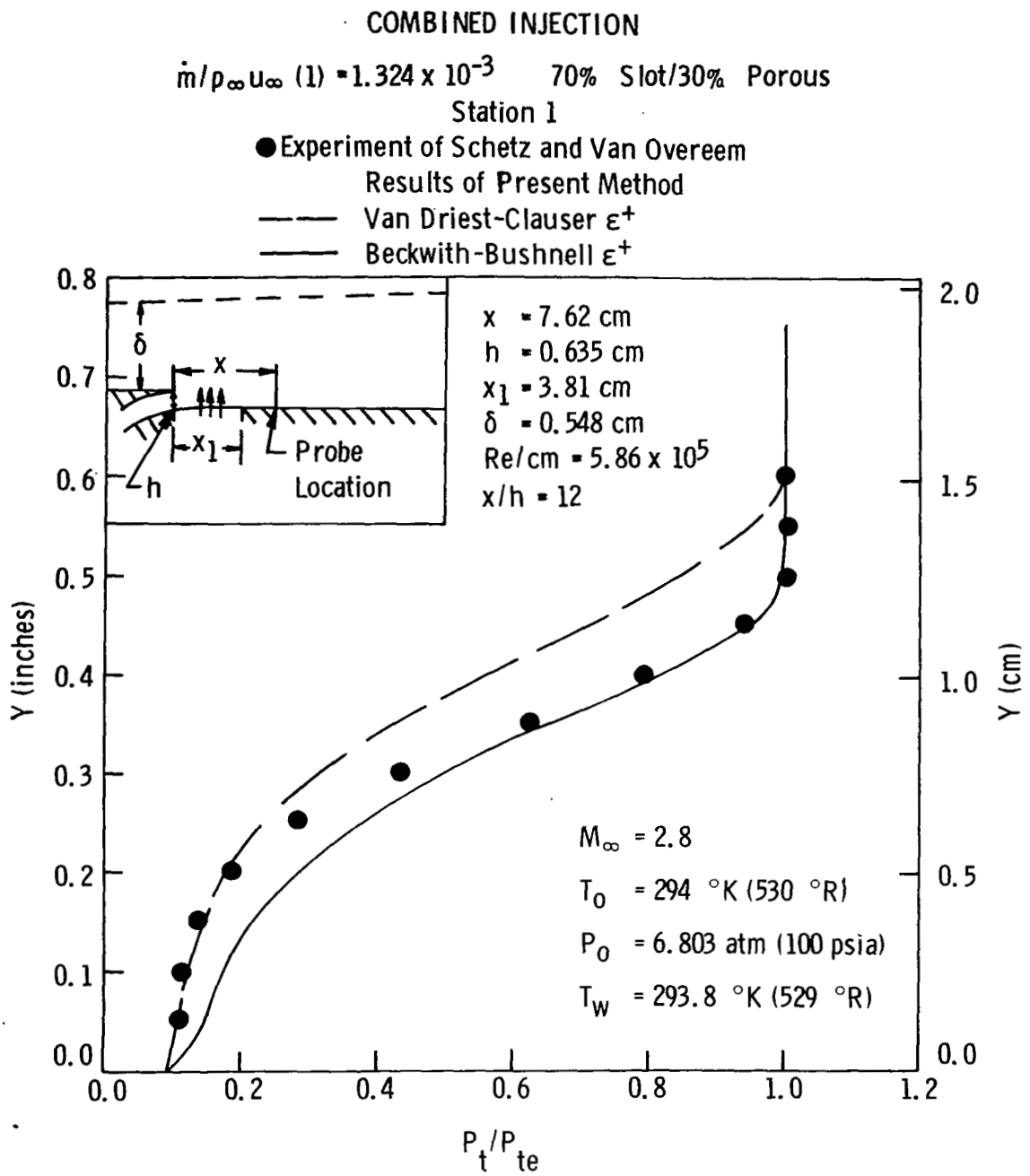

Figure 35: Combined Injection Pitot Pressure Profiles, Station 1

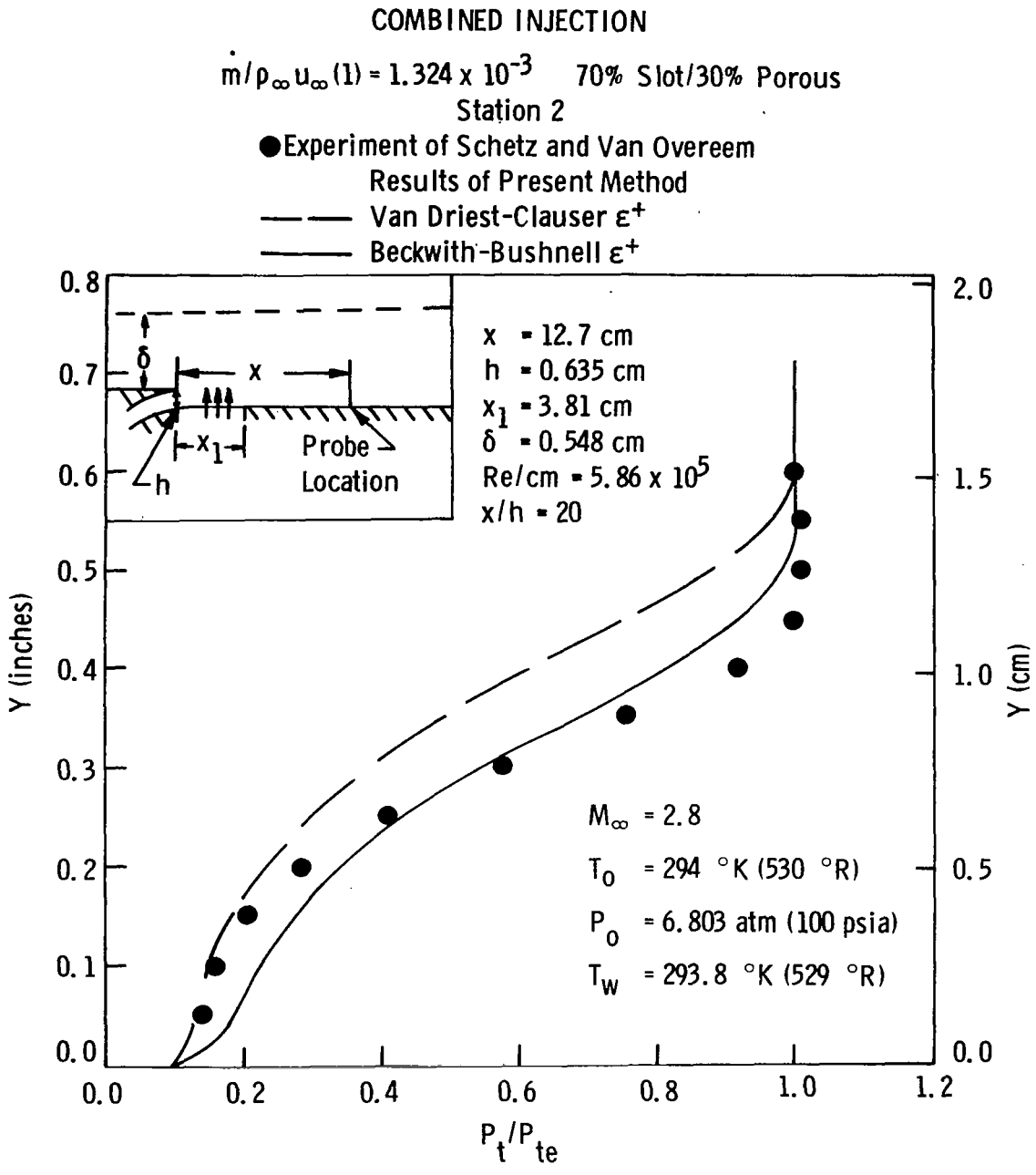

Figure 36: Combined Injection Pitot Pressure Profiles, Station 2

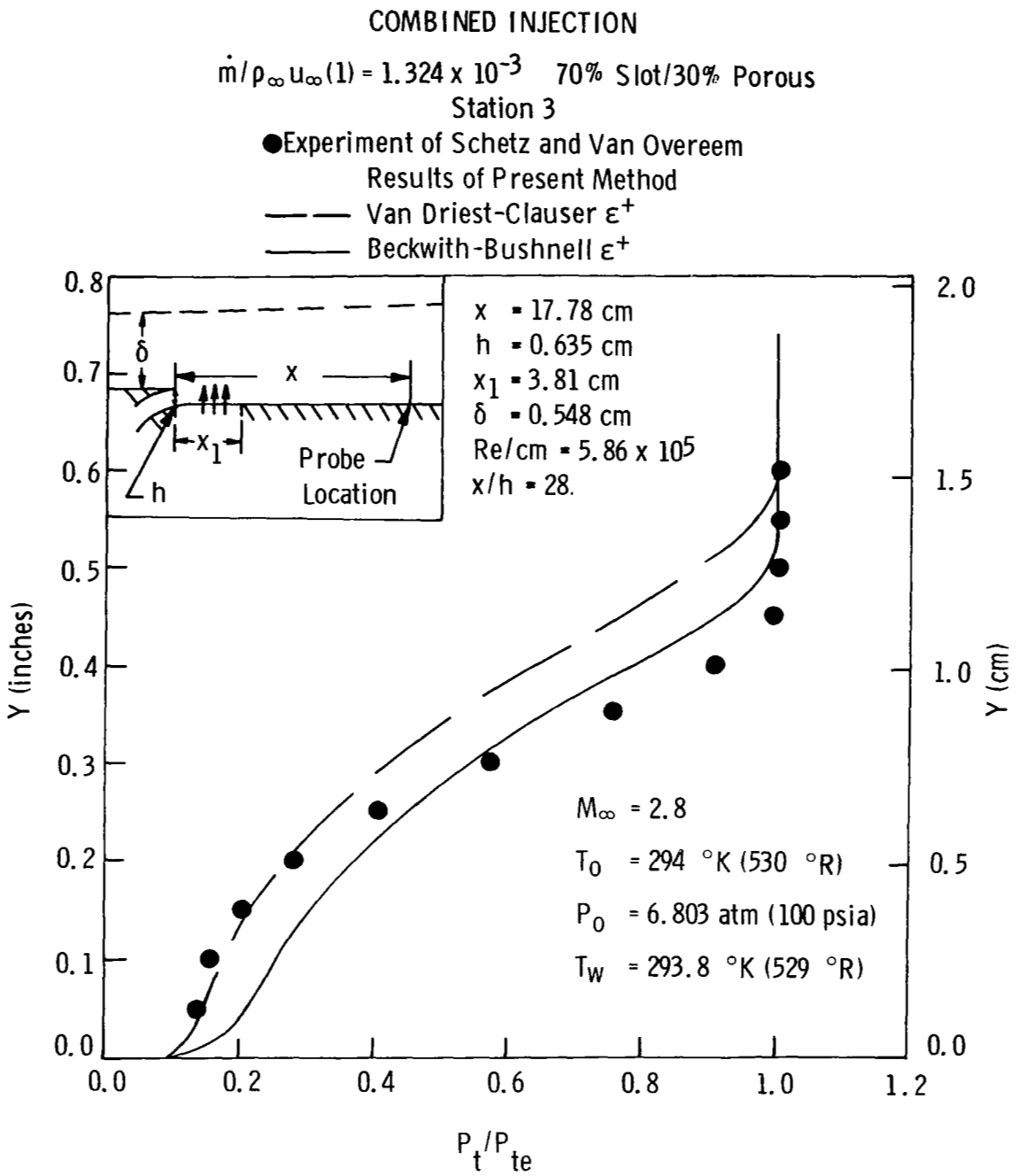

Figure 37: Combined Injection Pitot Pressure Profiles, Station 3

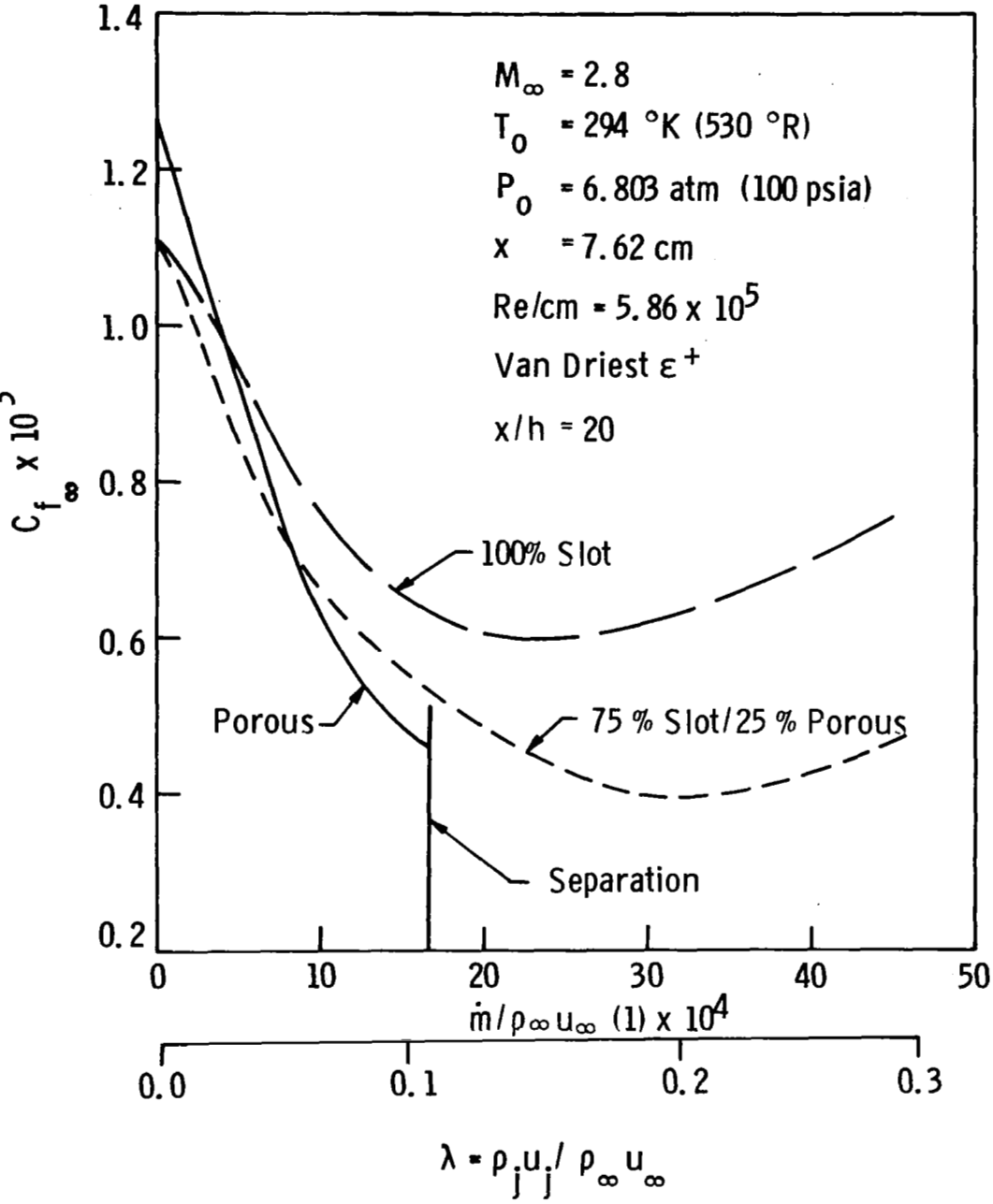

Figure 38: Comparison of Porous, Slot, and Combined Injection Skin Friction Variation with Mass Flow Rate